



NRL/MR/6410--08-9170

Computational Fluid Dynamics Studies of a Flapping Wing Nano Air Vehicle (NAV)

RAVI RAMAMURTI
WILLIAM C. SANDBERG
JASON GEDER

*Center for Reactive Flow and Dynamical Systems
Laboratory for Computational Physics and Fluid Dynamics*

December 31, 2008

REPORT DOCUMENTATION PAGE				Form Approved OMB No. 0704-0188	
Public reporting burden for this collection of information is estimated to average 1 hour per response, including the time for reviewing instructions, searching existing data sources, gathering and maintaining the data needed, and completing and reviewing this collection of information. Send comments regarding this burden estimate or any other aspect of this collection of information, including suggestions for reducing this burden to Department of Defense, Washington Headquarters Services, Directorate for Information Operations and Reports (0704-0188), 1215 Jefferson Davis Highway, Suite 1204, Arlington, VA 22202-4302. Respondents should be aware that notwithstanding any other provision of law, no person shall be subject to any penalty for failing to comply with a collection of information if it does not display a currently valid OMB control number. PLEASE DO NOT RETURN YOUR FORM TO THE ABOVE ADDRESS.					
1. REPORT DATE (DD-MM-YYYY) 31-12-2008		2. REPORT TYPE Memorandum Report		3. DATES COVERED (From - To)	
4. TITLE AND SUBTITLE Computational Fluid Dynamics Studies of a Flapping Wing Nano Air Vehicle (NAV)				5a. CONTRACT NUMBER 64-9173-A-7	
				5b. GRANT NUMBER	
				5c. PROGRAM ELEMENT NUMBER	
6. AUTHOR(S) Ravi Ramamurti, William C. Sandberg, and Jason Geder				5d. PROJECT NUMBER	
				5e. TASK NUMBER	
				5f. WORK UNIT NUMBER	
7. PERFORMING ORGANIZATION NAME(S) AND ADDRESS(ES) Naval Research Laboratory 4555 Overlook Avenue, SW Washington, DC 20375-5320				8. PERFORMING ORGANIZATION REPORT NUMBER NRL/MR/6410--08-9170	
9. SPONSORING / MONITORING AGENCY NAME(S) AND ADDRESS(ES) DARPA Technical Information Office (TIO) 3701 N. Fairfax Drive, Room 415 Arlington, VA 22203-1714				10. SPONSOR / MONITOR'S ACRONYM(S)	
				11. SPONSOR / MONITOR'S REPORT NUMBER(S)	
12. DISTRIBUTION / AVAILABILITY STATEMENT Approved for public release; distribution is unlimited.					
13. SUPPLEMENTARY NOTES					
14. ABSTRACT The goal of this project is to develop a Nano Air Vehicle (NAV) with a wing span of 7.5 cm. The computational fluid dynamics study is focused on the aerodynamic efficiency of the wings. The primary focus of the computational study is on the aerodynamic performance of the wings in order to obtain a near optimal kinematics of the wing while the NAV is in a hover mode. The secondary effort was of a more fundamental nature, in order to understand the differences between a rotating helicopter blade and a similarly designed wing undergoing a flapping motion.					
15. SUBJECT TERMS Flapping wing Hovering Incompressible flow Nano air vehicle Figure of merit Unstructured grid					
16. SECURITY CLASSIFICATION OF:			17. LIMITATION OF ABSTRACT UL	18. NUMBER OF PAGES 48	19a. NAME OF RESPONSIBLE PERSON Ravi Ramamurti
a. REPORT Unclassified	b. ABSTRACT Unclassified	c. THIS PAGE Unclassified			19b. TELEPHONE NUMBER (include area code) (202) 767-0608

Table of Contents

Introduction.....	1
Discussion of Results.....	2
Version 1.0.....	2
Kinematics Extraction from video.....	5
Version 2.0.....	8
Parametric Studies	9
1. Effect of Stroke angle (ϕ):	10
2. Effect of wing rotation angle (γ):.....	13
3. Effect of Phasing of wing rotation angle (β):	14
4. Effect of Frequency:	15
5. Aspect Ratio (AR) of the wing:	16
6. Camber and/or Twist:	17
7. Optimization using CFD and Design of Experiments:	19
8. Effect of Planform:	23
Propeller vs Flapping.....	24
Propeller as a flapper	26
Summary and Future Work.....	34
Acknowledgements.....	40
References.....	41
Appendix.....	42

CFD Studies of a flapping wing NAV

Introduction

There has been an increased level of activity in recent years in the development of small unmanned vehicles. Recent interest in Micro aerial vehicles (MAVs) and Nano Air Vehicles (NAVs) with wingspans of less than 15 cm and 7.5cm, respectively, has focused considerable attention on flapping foil propulsion. In the low Reynolds number ($5000 \leq Re \leq 50,000$) regimes accessed by such tiny aircraft, operating at very low speeds (~ 10 m/s), flapping wings are generally more dynamically advantageous than fixed wing configurations, particularly if operating in gusts or needing to avoid obstacles. Experimental and computational studies are also providing insight into the aerodynamics of actual biological flight, as well as suggesting biomimetic flapping wing configurations that, while they have no direct counterpart in nature, may be suited to NAVs. It is clear that a large number of creatures achieve their desired flight performance characteristics by utilizing either active or passive (or both) shape modifications.

This research effort is part of the Phase I for the DARPA program on NAVs. The goal of this effort is to develop an NAV with a wing span of 7.5cm. The NAV will be subjected to gust environments of less than 5 knots and majority of the mission will be in hover. In the Phase I of this project, multiple models and prototypes were developed. As a first step several lightweight miniature wings and linkages were created.

The computational fluid dynamics study focused on the aerodynamic efficiency of the wings. This included a significant modeling effort in order to study the complex interaction between the wing foils and the wing linkage. The majority of the effort was directed towards gaining insight to the design of high performance flapping wings. The primary focus of the computational study was on the aerodynamic performance of the wings in order to obtain a near optimal kinematics of the wing while the NAV is in a hover mode. The secondary effort was more of a fundamental nature, in order to understand the differences between a rotating helicopter blade and a similarly designed wing undergoing a flapping motion.

An unstructured grid-based unsteady Navier-Stokes solver with automatic adaptive remeshing, called FEFLO, was used to compute the flow about the flapping wing through several complete cycles of oscillation for each of the cases studied. Ramamurti and Sandberg [1] computed 2-D flow about pitching and heaving airfoils and compared their results with the experimental work of Anderson [2]. While 2-D wing section investigations can yield useful insights on the coupled pitching and heaving dynamics, it is essential to carry out 3-D computations to understand the influence of spanwise flow. We chose to pursue the fruit fly for computational investigations since both detailed wing kinematics and corresponding force data were available. Ramamurti and Sandberg [3] have computed the force production in *Drosophila* and obtained nearly exact agreement with the measured force data of Dickinson et al. [4] Ramamurti and Sandberg [5] have also carried out 3-D unsteady computations of insect maneuvering. The computed force production throughout the saccade maneuver again was in nearly exact agreement with measured forces of Fry et al. [6]. The first few hover cycles of this fruitfly was analyzed and yielded a figure of merit of 20%.

Discussion of Results

Version 1.0

Initial computations were performed on the first NAV wing, version 1.0, designed by David Cylinder of Princeton Plasma Physics Laboratory. The kinematics from the RoboFly experiment [4] is used as the initial kinematics. The wing stroke amplitude was scaled by a factor of 0.75 from the original RoboFly kinematics, Fig 1b. The wing configuration and the kinematics are shown in Fig. 1a-c. 3-D unsteady flow simulations (run 1.0) were conducted at a flapping frequency of 5Hz and 80Hz for several flapping cycles. At a flapping frequency of 5Hz, the results show that one wing produces a mean lift of 0.268 mN and a mean forward force of nearly zero. This implies that two wings can generate enough lift to hold 54mg. As the frequency is increased to 80Hz, Fig. 3, the mean thrust increases by a factor nearly proportional to the square of the frequency ratios to 0.0626 N while the mean forward thrust remaining nearly zero. At this frequency, two wings can produce enough lift to support a 13g vehicle. The time history of the aerodynamic power input to the wing and the center of pressure on the wing were computed and are shown in Fig. 4. The mean power input to one wing at 80Hz is nearly 1.01 W and the mean center of pressure is located at 70% of the wing span from the hinge point.

Instead of the version 1.0 wing planform, the fruitfly *Drosophila* wing shown in Fig. 5a was used (run1.1). The kinematics were maintained to be the same as in Fig.1 and results showed that there was a slight reduction in the mean thrust produced by the fruitfly wing to 0.0481 N, Fig 5c, but the mean aerodynamic power input to the wing is reduced by nearly 40% to 0.6 W, shown in Fig 5b. Hence, the planform was modified to remove a small region near the trailing edge portion of the root of the wing. Figure 6 shows a few modifications to this wing.

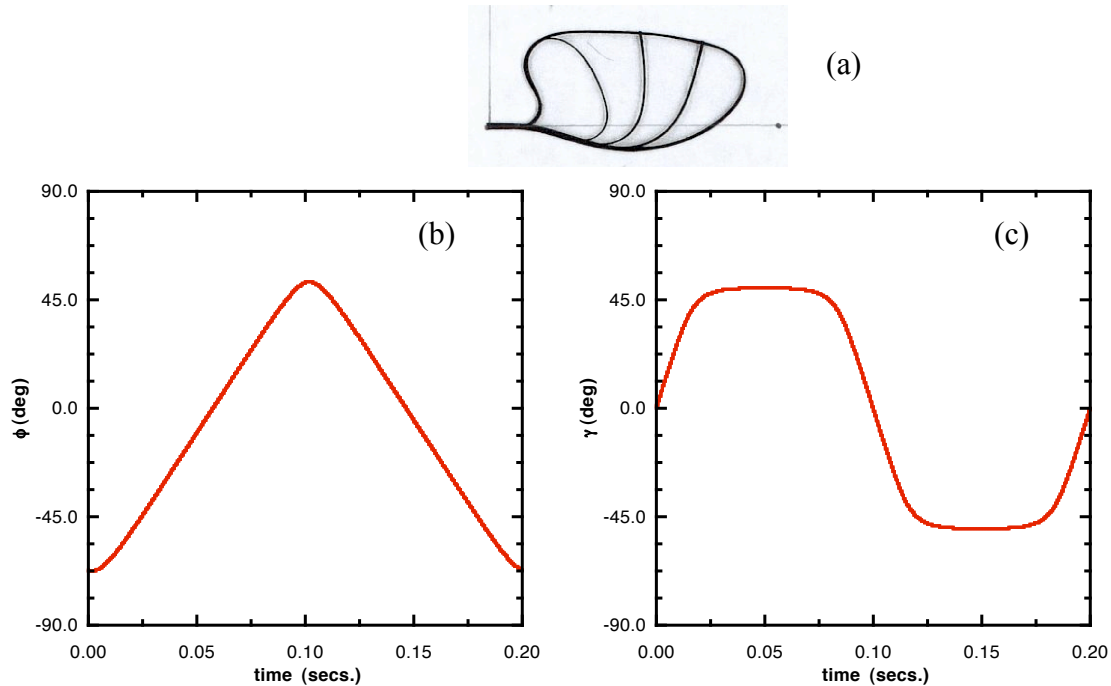


Fig. 1. Wing planform and kinematics for version1.0.

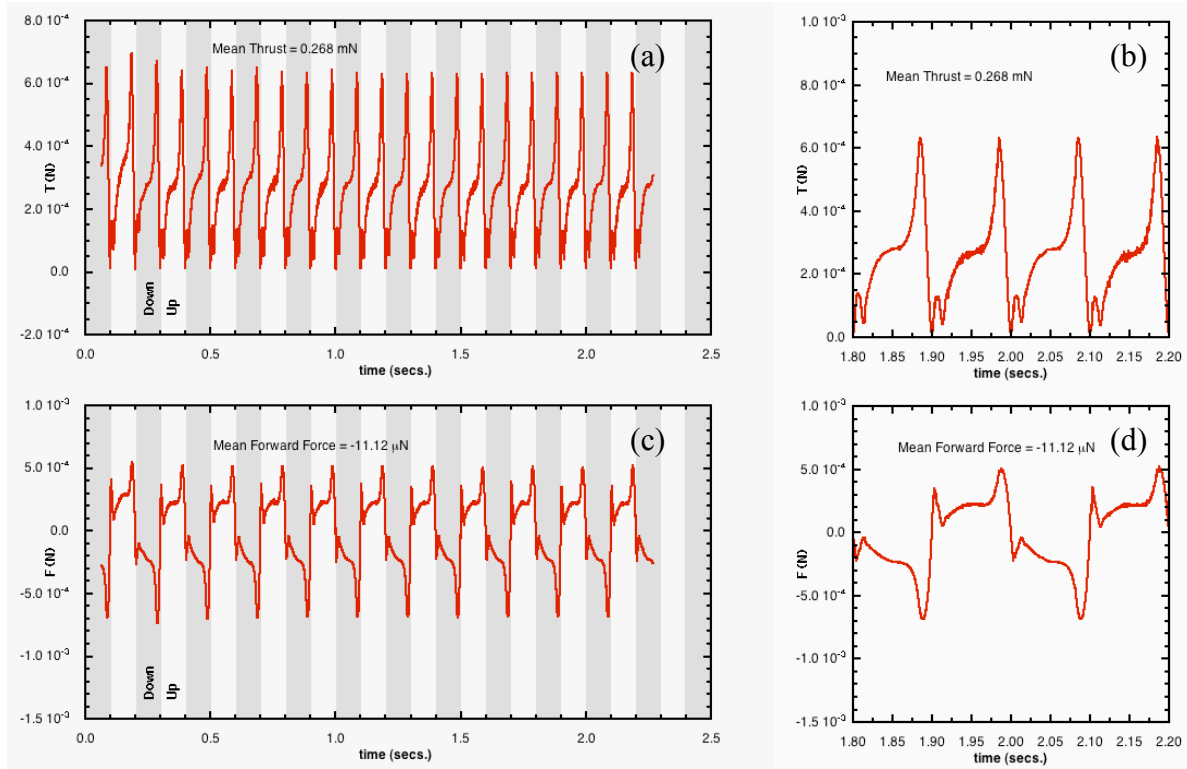


Fig. 2. Force production from a version 1.0 wing flapping at 5Hz (run1.0), (a) time history of thrust force, (b) thrust for 2 flapping cycles, (c) time history of forward force and (d) forward force for 2 flapping cycles.

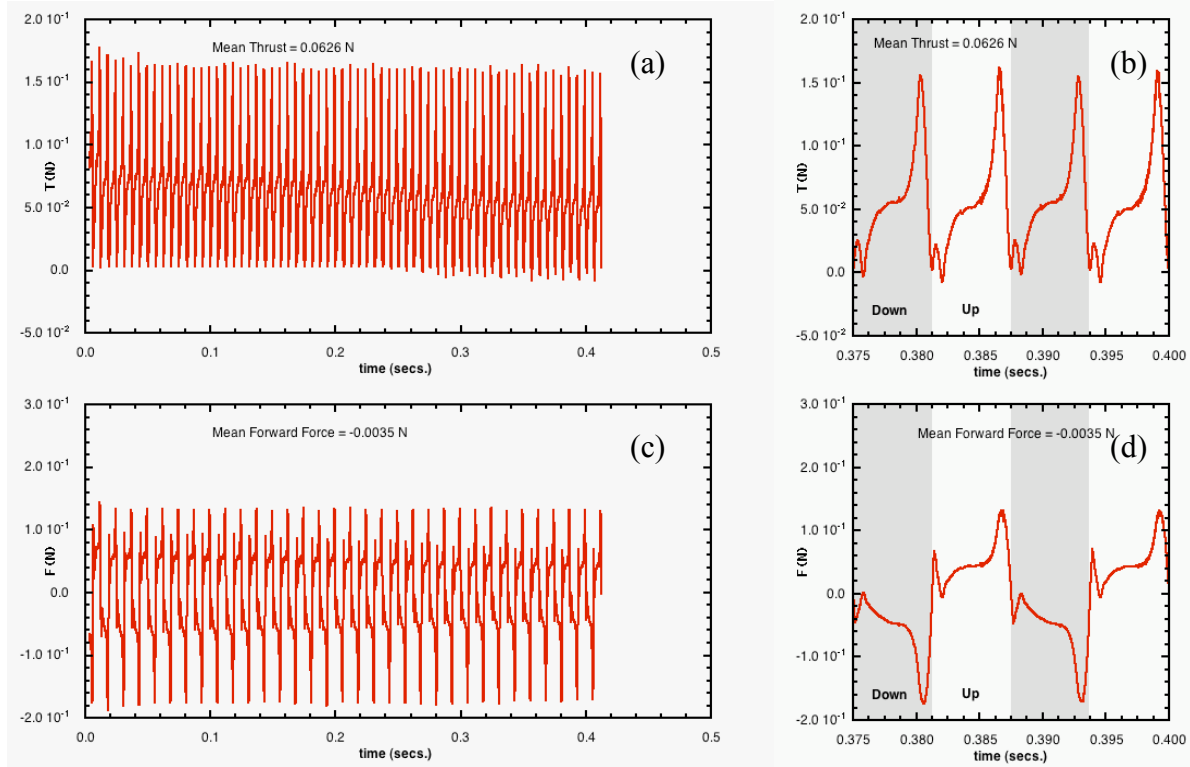


Fig. 3. Force production from a version 1.0 (run1.0) wing flapping at 80Hz.

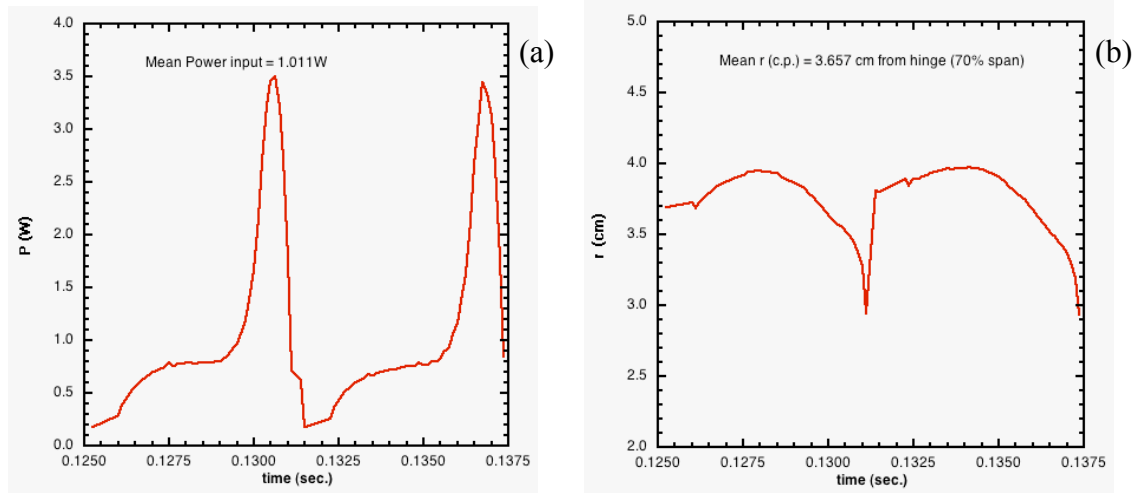


Fig. 4. (a) Aerodynamic power input and (b) center of pressure on a wing flapping at 80Hz.

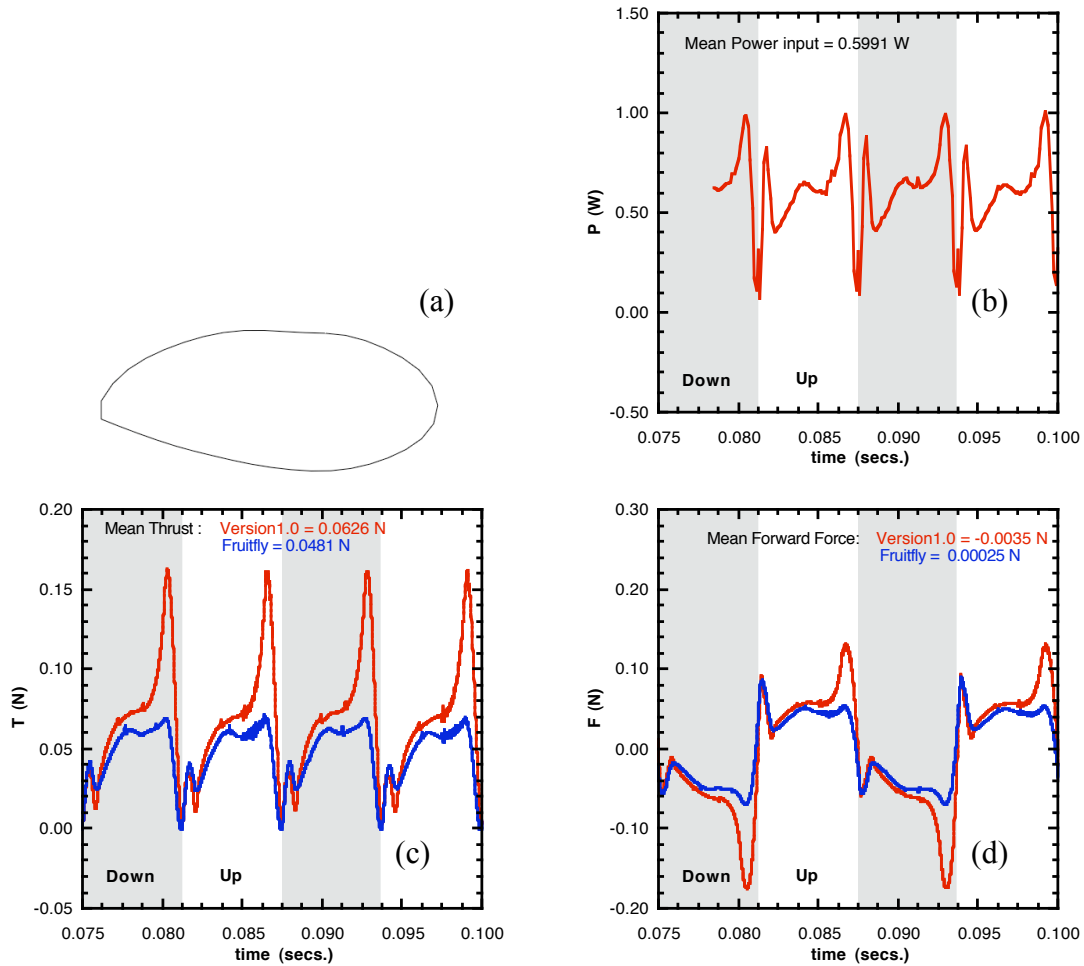


Fig. 5. Results of a flapping *Drosophila* wing, $f=80$ Hz, (a) planform of the wing, run1.1, (b) aerodynamic power input to the wing, time histories of (c) thrust and (d) forward force.

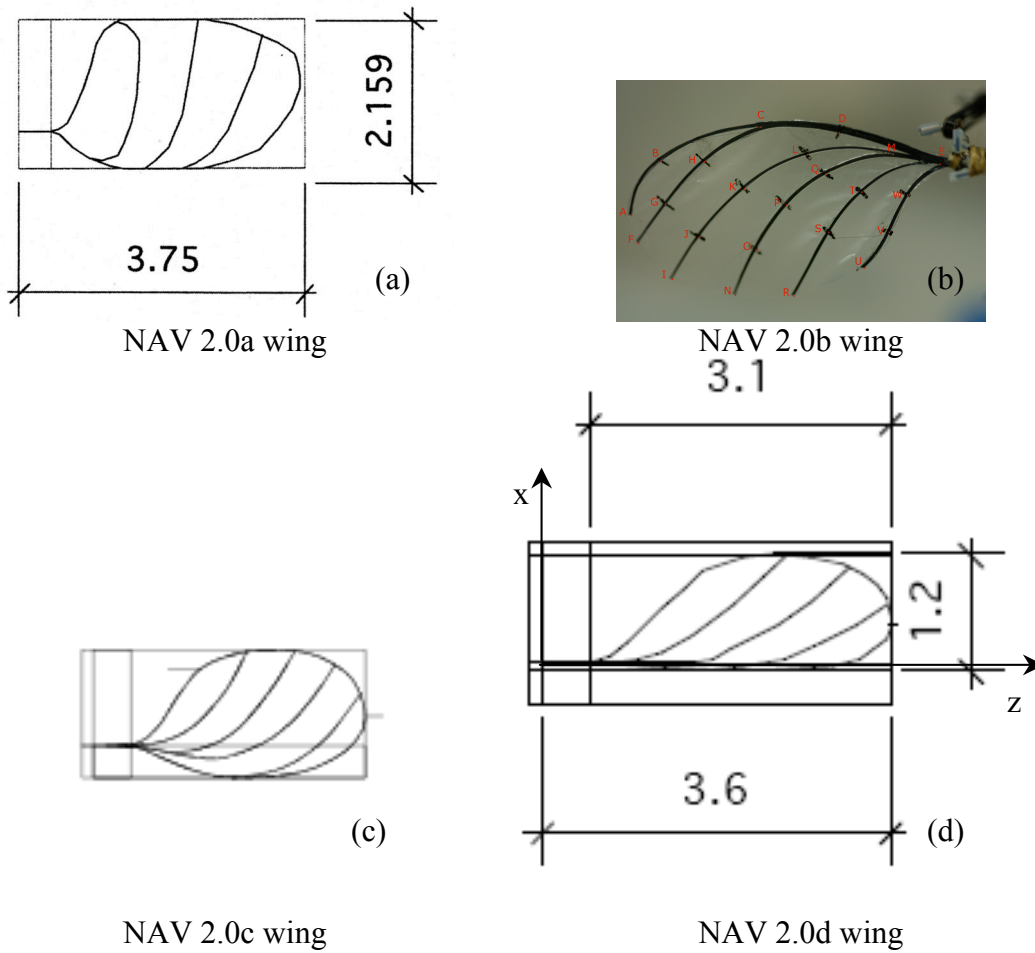


Fig 6. Modified Wing Shapes

Kinematics Extraction from video

The first linkage configuration that was built and tested was a double crank rocker design. The double crank rocker was a planar mechanism and had the advantage of being simple, which makes it amenable for miniaturization. A single rotor drove a four bar linkage for each wing. However, the double crank-rocker mechanism has an inherent asymmetry due to the way the two four-bar linkages need to be offset when attached to the rotor.

High speed video was obtained for this mechanism with the wing planform shown in Fig. 6a. One of the slowest runs with least wing twist and vibration was chosen. Since there was only one camera view and no calibration of the camera was available, a simple digitization of the frames was performed. On each frame of the video 4 points were selected as shown in Fig. 7a. As the camera view was normal to the wing stroke plane, two points on the wing root (points 1 and 2) define the wing stroke angle. The wing stroke angle $\phi(t)$ was computed directly from 2-D pixel coordinates as in Eq. 1a.

In order to obtain the angle of attack or the wing rotation angle two points were selected in the mid span of the wing (points 3 and 4), one at the leading edge and the other on the trailing edge of the wing. The angle of attack was computed from 2-D pixel coordinates using knowledge of the pixel distance between two points when the wing plane is parallel to the image

plane, Fig. 7b, and by scaling the distance in real world coordinates (cm) between the same points. Using the video, we can measure the pixel distance from root to the tip of the wing. We can also measure the distance in cm from root to the tip of the wing, as well as the distance in cm from point 3 to point 4. Knowing the distance in pixels from leading to trailing edge point for each frame throughout the stroke, we can calculate the angle of attack $\alpha(t)$ using the ratio of measured distance and the distance if the wing is parallel to the view plane, as in Eq. 1b. The wing rotation angle measured from the vertical axis, $\gamma(t)$, is given by Eq. 1c.

The kinematics obtained thus is shown in Fig. 8a and b. The 3-D unsteady flow was simulated using the experimental kinematics shown by the blue curves in Fig. 8, run1.2, at a wing flapping frequency of 60Hz. The thrust and forward force time history is shown in Fig. 9. These traces show more force reversals in each of the up and down strokes. Hence, the raw kinematics obtained from the video is smoothed based on the angular accelerations. The smoothed kinematics is shown by the green curve in Fig. 8. The resultant force time history is shown in Fig. 10 and we can see the high frequency oscillations are eliminated. The mean thrust or lift per wing for this configuration is only 0.003 N, shown in Fig. 11. Comparing the present kinematics with that of the Robofly, it is clear that the wing rotation angle is not properly phased with respect to stroke reversal. Hence, the kinematics was modified so that the $\gamma(t)$ closely matched that of the Robofly, run1.2.2, as shown by the black curve in Fig. 8. The unsteady flow simulation using this modified kinematics showed a four-fold improvement in the lift generated. Figure 11 shows the mean lift for this case is 0.0131 N.

$$\begin{aligned}\phi(t) &= \tan^{-1}\left(\frac{x_2 - x_1}{y_2 - y_1}\right), \\ \alpha(t) &= \sin^{-1}\left(\frac{((x_4 - x_3)^2 + (y_4 - y_3)^2 - \bar{x}^2)^{1/2}}{\bar{y}}\right), \\ \gamma(t) &= \frac{\pi}{2} - \alpha(t)\end{aligned}\tag{1a-c}$$

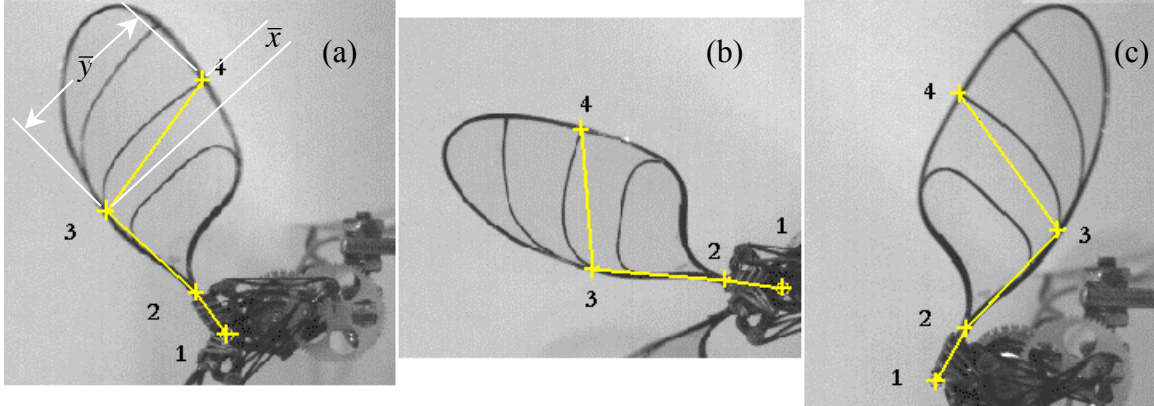


Fig. 7. Extracting kinematics from the video of the double crank-rocker mechanism.

Next, a laminar viscous solution was obtained with this kinematics, run1.2.3, to study the effect of viscosity. The Reynolds number for this case is approximately 9050, based on the mean wing tip velocity and a mean chord of 1.73 cm. It is clear from Fig. 11, that the force time history remains nearly unchanged for this case. This is mainly due to the fact that the forces generated are inertially dominated arising from the large motion of the high at relatively high angles of

attack. Earlier computations on the Robofly experiment [3] also showed similar results for the effect of viscosity. Hence, in this study inviscid simulations were deemed sufficient for parametric studies and optimization of the wing kinematics.

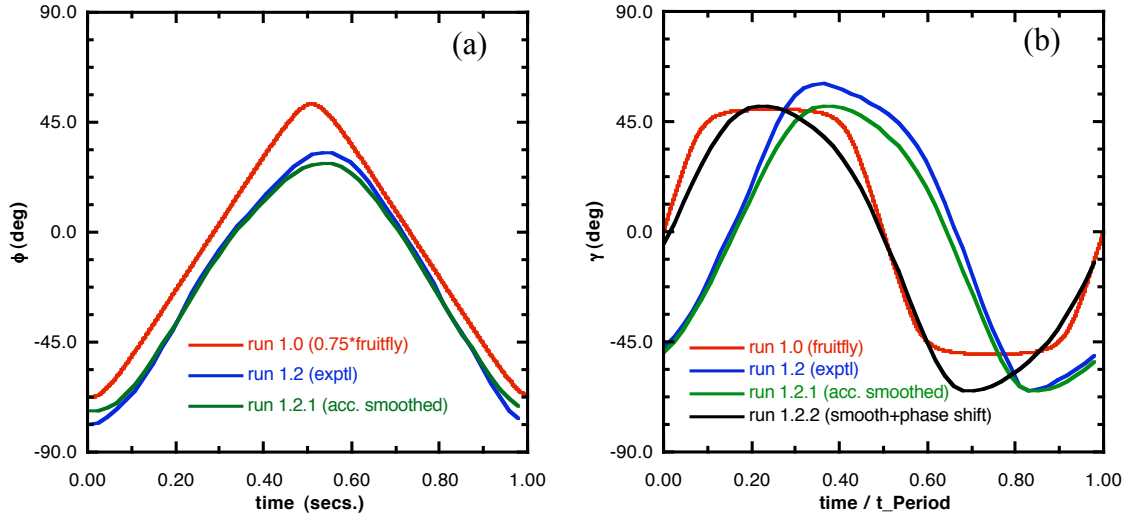


Fig. 8. Kinematics obtained from the double crank rocker mechanism.

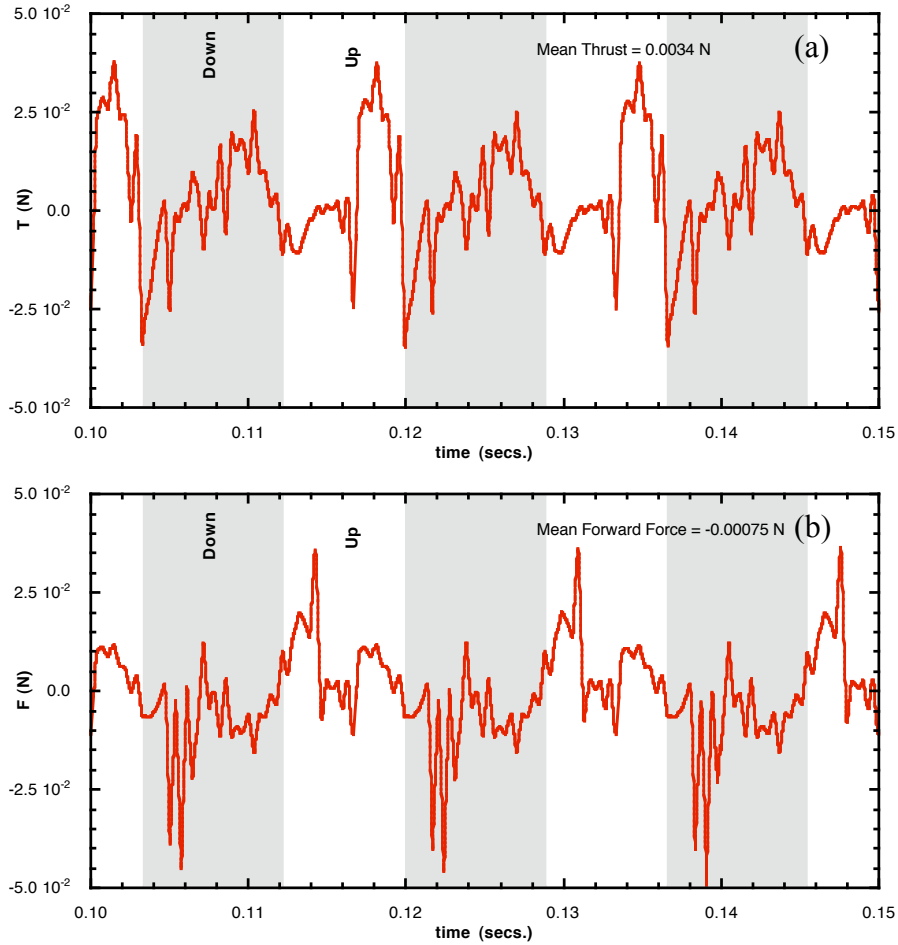


Fig. 9. Force production of Version 1.0 with experimental kinematics, $f = 60\text{Hz}$, run 1.2.

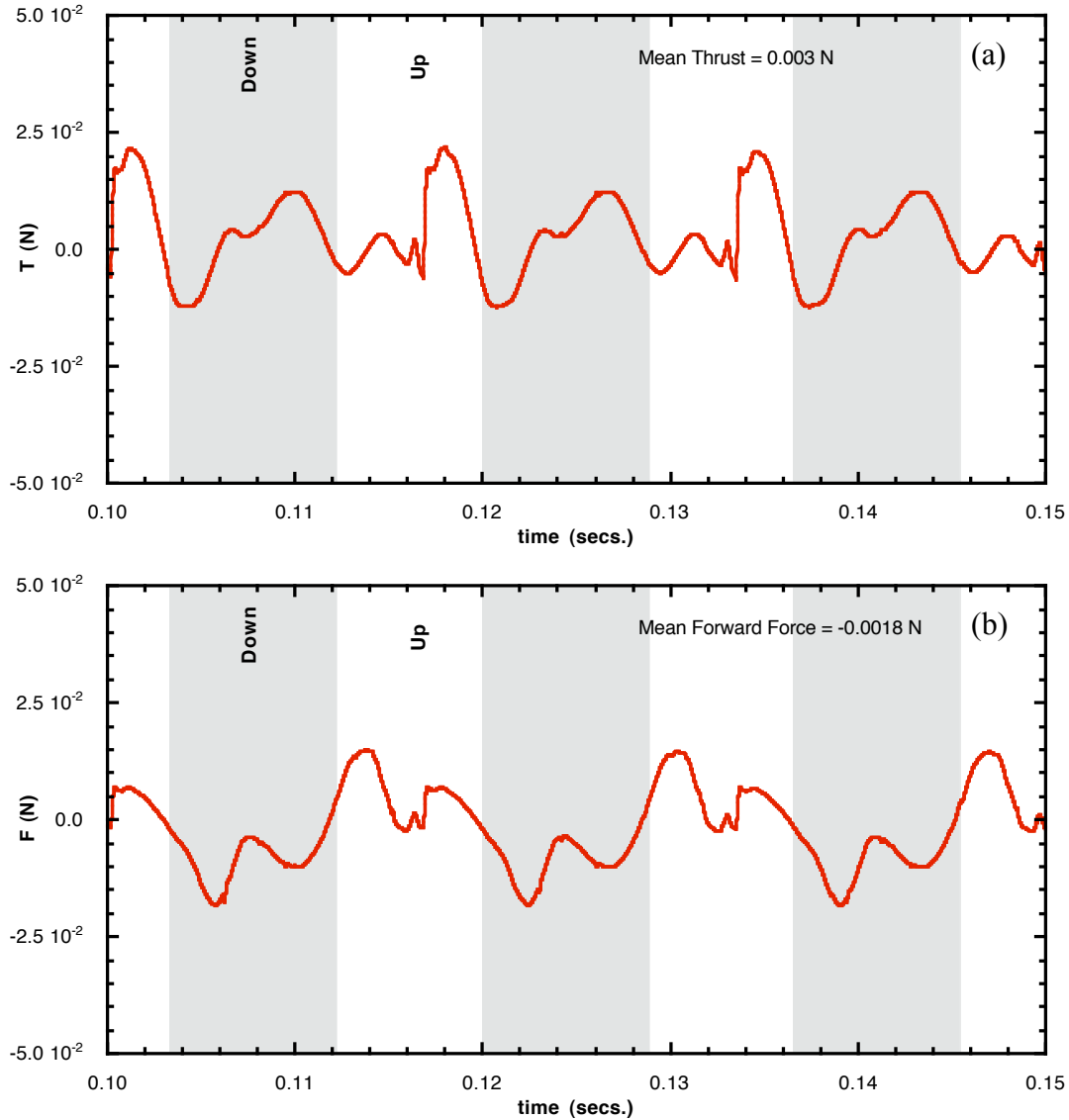


Fig. 10. Force production of Version 1.0 with smoothed kinematics, $f = 60\text{Hz}$, run1.2.1.

Version 2.0

The next generation of the linkage mechanism that was developed was based on a bicycle drive. This configuration eliminated the asymmetries present in the double crank drive, and the right and left wings are driven symmetrically with in manufacturing tolerance, while keeping the mechanism is robust and lightweight. High speed video of the wing flapping at 62.3Hz were taken by Caltech researchers with this mechanism for wing versions b and c shown in Fig. 6b and c. The wing and the linkage mechanism and the two angles of rotations are shown in Fig. 12a and b. The kinematics was obtained by digitizing the first 94 frames of NAV2.0c_v3.0 run and is shown in Fig. 13a and b. The kinematics was smoothed based on the angular accelerations and used with the wing planform of version d shown in Fig. 6d. This will be our baseline configuration to improve thrust and efficiency. The mean thrust for one wing flapping at

62.3Hz, run2.0 is 0.01164 N, shown in Fig. 14. Note that there is only one peak during each up and downstroke.

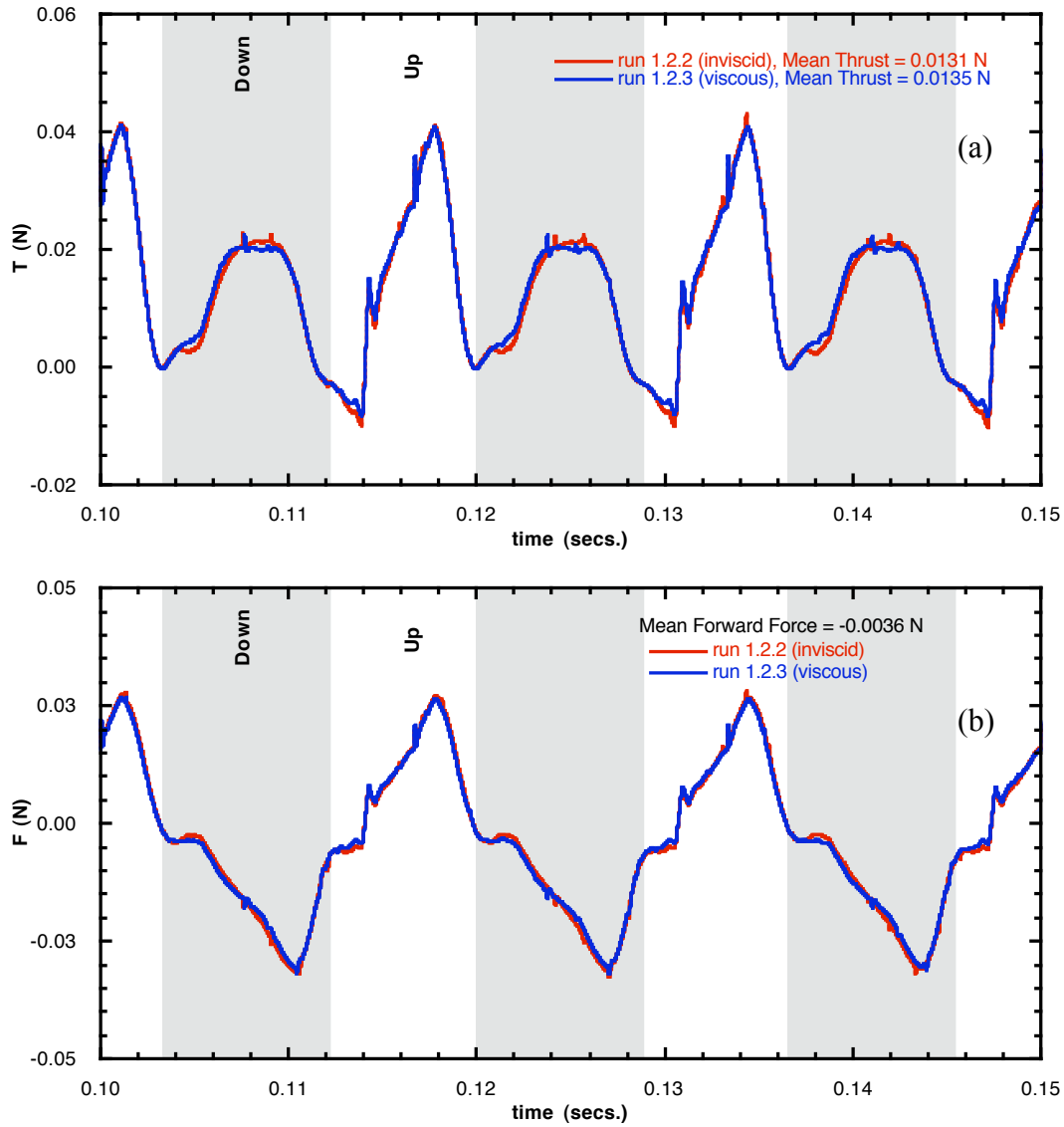


Fig. 11. Force production of a wing flapping with properly phased kinematics, $f = 60$ Hz.

Parametric Studies

We undertook a systematic study in an effort to study the effect of various parameters that govern the kinematics in an attempt to optimize the kinematics for hovering flight. The possible kinematic parameters include stroke angle $\phi(t)$, the wing rotation angle $\gamma(t)$, the wing flapping frequency, the aspect ratio of the planform, the camber and twist of the wing.

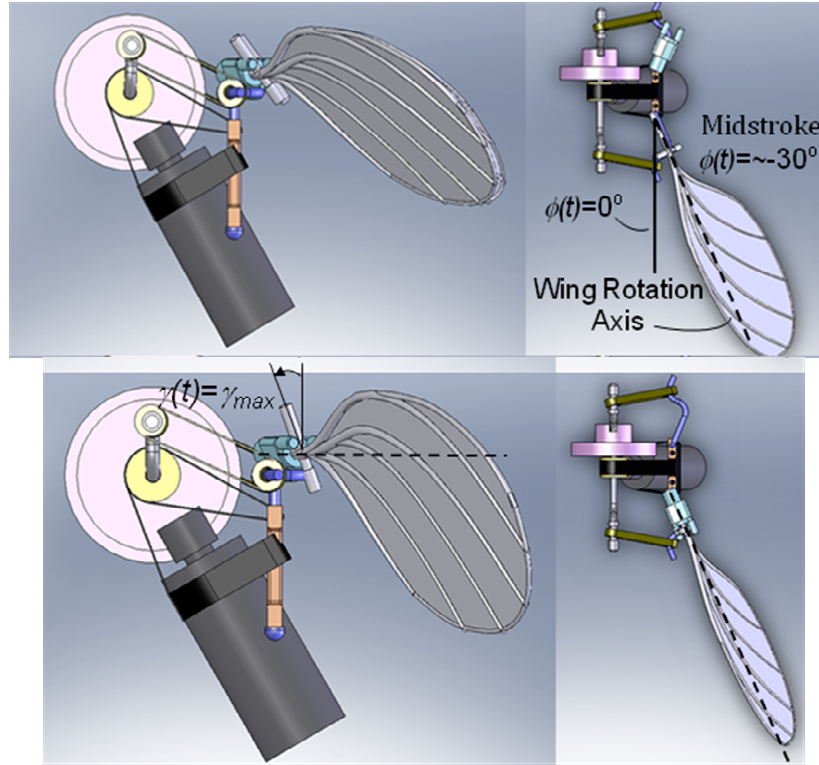


Fig. 12. Bicycle drive mechanism, NAV2.0c, showing the two wing rotation angles.

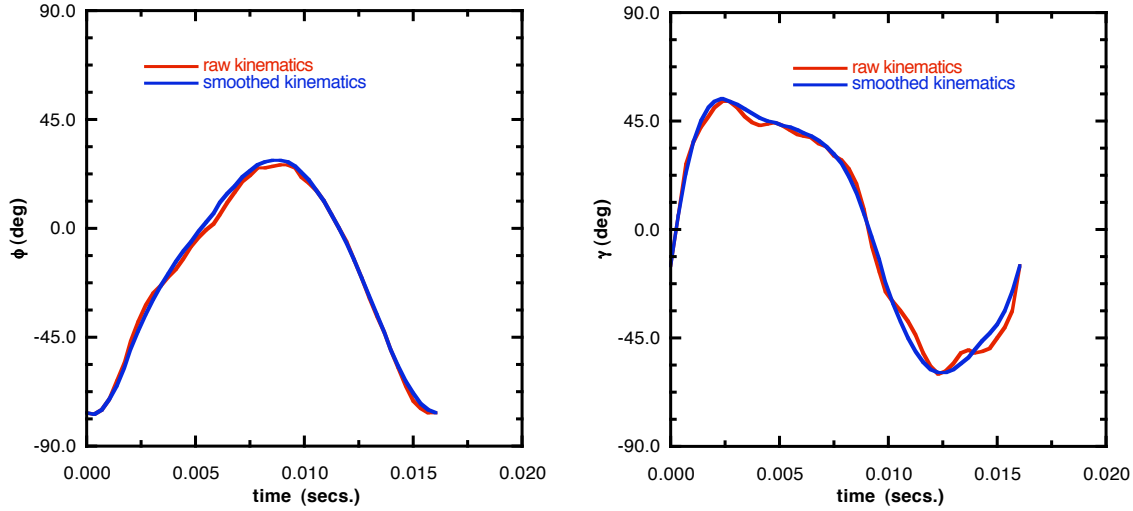


Fig. 13. Kinematics of NAV2.0c.

1. Effect of Stroke angle (ϕ):

The initial stroke angle variation $\phi_0(t)$ is obtained from NAV2.0c_v3.0 kinematics (red line in Fig. 15). The amplitude of the stroke angle is varied as follows:

$$\begin{aligned}
 \phi(t) &= \phi_{fac} * \phi_0(t), \\
 \phi_{fac} = 1.00 &\Rightarrow \phi_{max} - \phi_{min} = 104.6^\circ \text{ (NAV2.0c_v3.0)} \\
 &= 1.25 \Rightarrow \phi_{max} - \phi_{min} = 130.8^\circ \\
 &= 1.45 \Rightarrow \phi_{max} - \phi_{min} = 151.7^\circ
 \end{aligned} \tag{2}$$

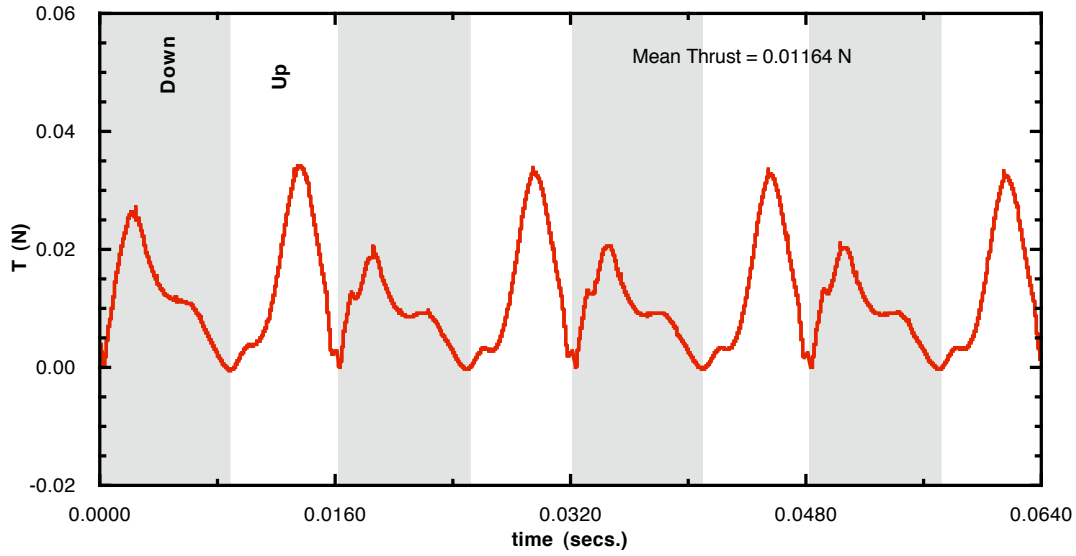


Fig. 14. Thrust time history for the baseline configuration.

Figure 16a shows the variation of thrust time history for the different amplitudes of stroke angle considered. The mean thrust increases from 0.01164N to 0.0249N by increasing the stroke amplitude from the baseline value of 104.6° to 151.7° . This increased amplitude was deemed mechanically feasible and therefore was fixed for our CFD coupled with Design of Experiments simulations.

The thrust produced and the aerodynamic power were computed by integrating the unsteady pressure on the surface of the wing and are non-dimensionalized as follows:

$$T = \hat{\mathbf{h}} \cdot \int p \mathbf{n} dA$$

$$P_{aero} = \mathbf{F} \cdot \mathbf{w} = \int p \mathbf{w} \cdot \mathbf{n} dA \quad (3a-e)$$

$$C_T = \frac{T}{\frac{1}{2} \rho V_{tip}^2 A_w},$$

$$C_P = \frac{P_{aero}}{\frac{1}{2} \rho V_{tip}^3 A_w}, \quad \text{where}$$

$$V_{tip} = 2(\phi_{max} - \phi_{min})Rf$$

where p is the computed pressure on the wing surface, \mathbf{w} is the velocity of the wing, \mathbf{n} is the normal vector the wing surface, $\hat{\mathbf{h}}$ is the unit normal in the hover direction and V_{tip} is the mean tip speed of the wing. In terms of the non-dimensional thrust coefficient all the three curves nearly collapse into one as shown in Fig. 16b. The mean thrust coefficient per flapping cycle is approximately 0.52.

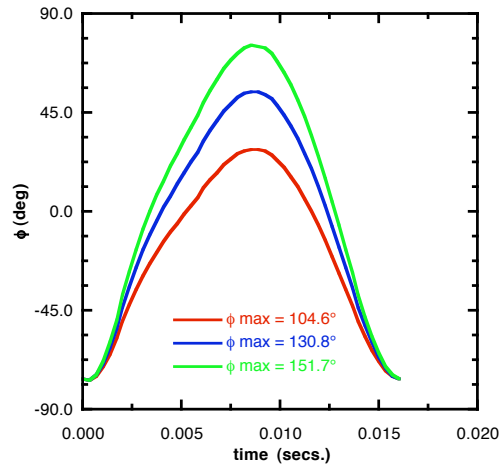


Fig. 15. Stroke angle variation.

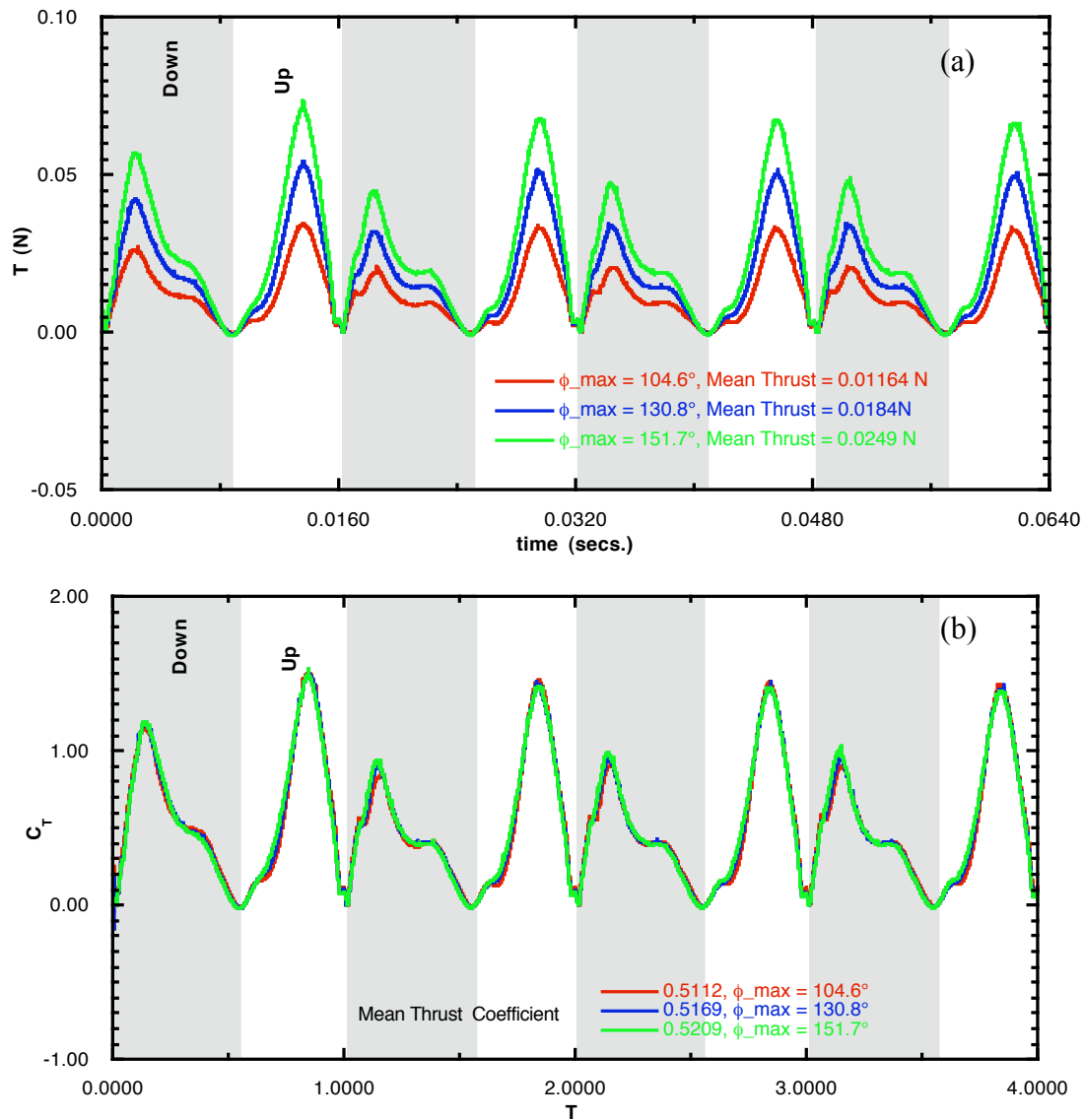


Fig. 16. Variation of thrust and coefficient of thrust time history with stroke amplitude.

2. Effect of wing rotation angle (γ):

The baseline wing rotation angle variation, $\gamma_0(t)$, is obtained from NAV2.0c_v3.0 kinematics (red line in Fig. 17). The mid stroke wing rotation angle was varied as follows:

$$\begin{aligned}\gamma(t) &= \gamma_{fac} * \gamma_0(t), \\ \gamma_{fac} &= 1.00 \Rightarrow \gamma_{\min} = -60^\circ, \gamma_{\max} = 54^\circ \text{ (NAV2.0c_v3.0)} \\ &= 0.75 \Rightarrow \gamma_{\min} = -45^\circ, \gamma_{\max} = 40.5^\circ \\ &= 0.50 \Rightarrow \gamma_{\min} = -30^\circ, \gamma_{\max} = 27^\circ\end{aligned}\quad (4)$$

Figure 18 show the variation of thrust for the three wing rotations angle distributions considered. As the mid stroke wing rotation angle is reduced the mean thrust increases slightly from 0.0249 N to 0.0253 N mainly due to the improved thrust during the downstroke. Further reduction in wing rotation angle reduces the thrust during both up and downstrokes yielding a mean value of 0.0207 N.

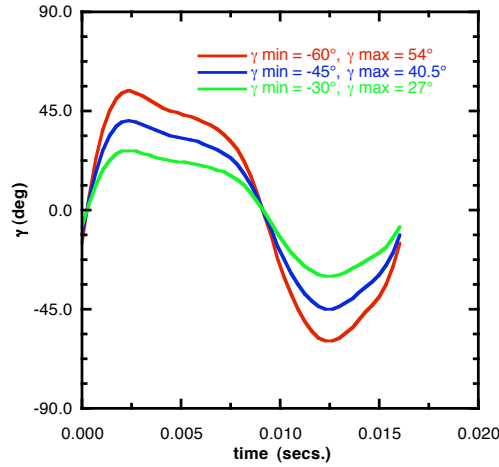


Fig. 17. Wing rotation angle variation.

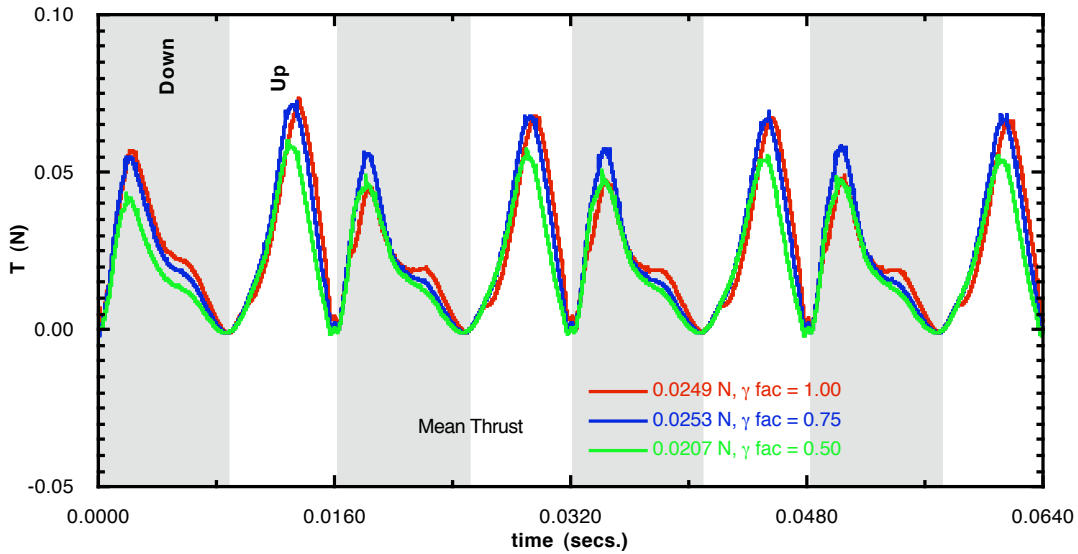


Fig. 18. Thrust variation with wing rotation angle, run2.01 (red), run2.04 (blue) and run2.07 (green).

3. Effect of Phasing of wing rotation angle (β):

The stroke angle for this study will be with $\phi_{\text{fac}} = 1.45$. The NAV2.0c kinematics shown in Fig. 19 (red line w.r.t. black line) exhibits delayed rotation in the wing rotation angle, i.e., the wing rotation peaks much after the stroke reversal. Therefore, the wing rotation was shifted to be in phase to match the peak of the stroke angle (blue line). This was termed symmetric with a phase angle $\beta = 0^\circ$. The wing rotation was further modified to advance the rotation (green line), corresponding to a $\beta = 15.3^\circ$. The base line $\gamma(t)$ with $\gamma_{\text{fac}} = 1.0$ was used first.

Figure 20 shows the thrust variation with the phasing of the wing rotation angle w.r.t. the stroke angle and the effect is significant. The baseline wing rotation ($\gamma_0(t)$) is approximately 15.3° delayed and yields a mean thrust of 0.0249 N. When the wing rotation is symmetric, the mean thrust improves to 0.0284 N and advancing the wing rotation by 15.3° improves the mean thrust to 0.0294 N, nearly 18% improvement over the baseline wing rotation. In the advanced rotation case, the appearance of a second thrust peak in the end of the downstroke or beginning of the upstroke suggests the wake capture effect.

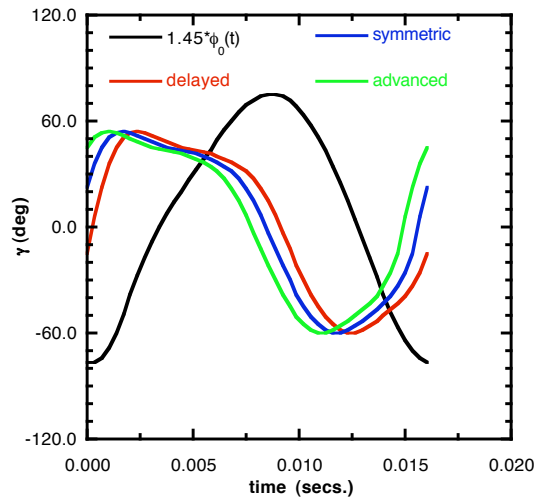


Fig. 19. Phasing of wing rotation angle w.r.t. stroke angle.

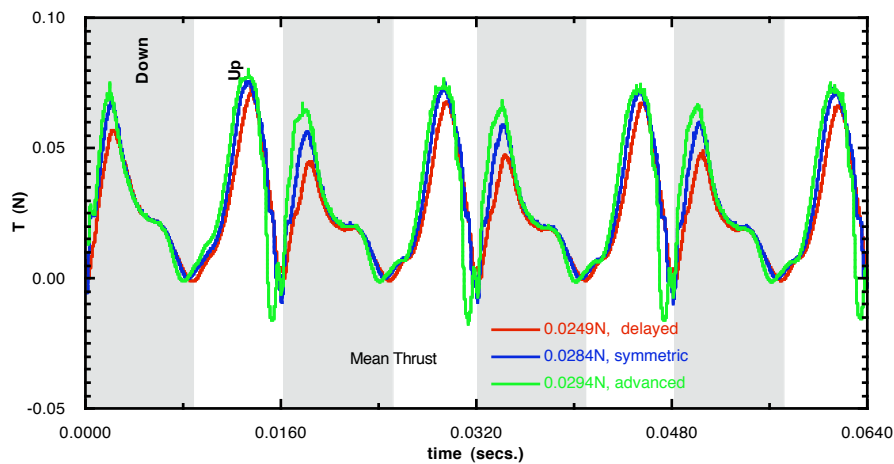


Fig. 20. Effect of phasing of wing rotation angle on the thrust time history, run 2.01(red), run2.02 (blue) and run2.03 (green).

Further parametric studies were performed varying both the γ factor and the phasing. Table 1 shows the variation of the mean thrust. For the symmetric and advanced cases, reducing the mid stroke wing rotation angle results in a reduction in the mean thrust. These results show that we can get nearly 6gf of lift from 2 wings at 62.3Hz. From our frequency scaling analysis, we can get 10gf at 80Hz. These results were used by the Design of Experiments (DOE) analysis. From that analysis, the next set of parametric studies increasing the wing rotation factor to 1.25 and the phasing to 30.6° are obtained.

γ factor	delayed (-15.3°)	Symmetric (0°)	advanced (15.3°)
1.00	0.0249	0.0284	0.0294
0.75	0.0253	0.0280	0.0287
0.50	0.0207	0.0224	0.0219

Table 1. Mean Thrust (N) variation with mid stroke α and phasing β .

4. Effect of Frequency:

In order to test the effect of flapping frequency on the thrust/force produced and the power input to the wing, the case with the chord factor γ of 1.0 with a phase shift of 15.3° and a rigid fin was selected. The frequency was increased from 62.3Hz to 72.5Hz so that the thrust produced by one wing is approximately 5gf, shown in Fig. 21.

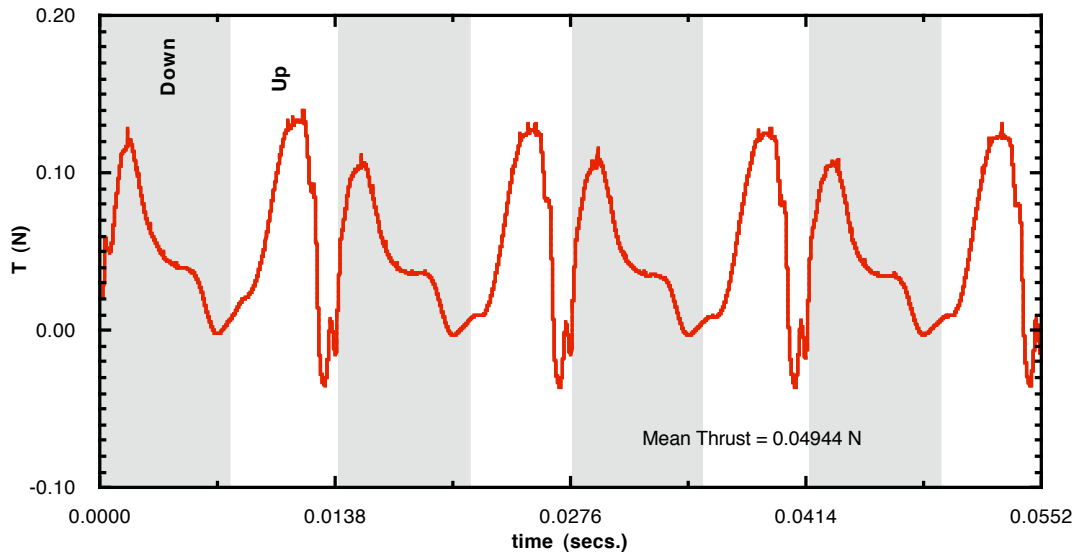


Fig. 21. Thrust variation at a flapping frequency $f = 72.5\text{Hz}$. run5.04.1.

In terms of the non-dimensional coefficients the thrust and the power distributions for the two frequencies tested collapse into a single curve, as shown in Fig. 22a and b. The mean thrust coefficient is approximately 0.61 and the mean power coefficient is 0.83.

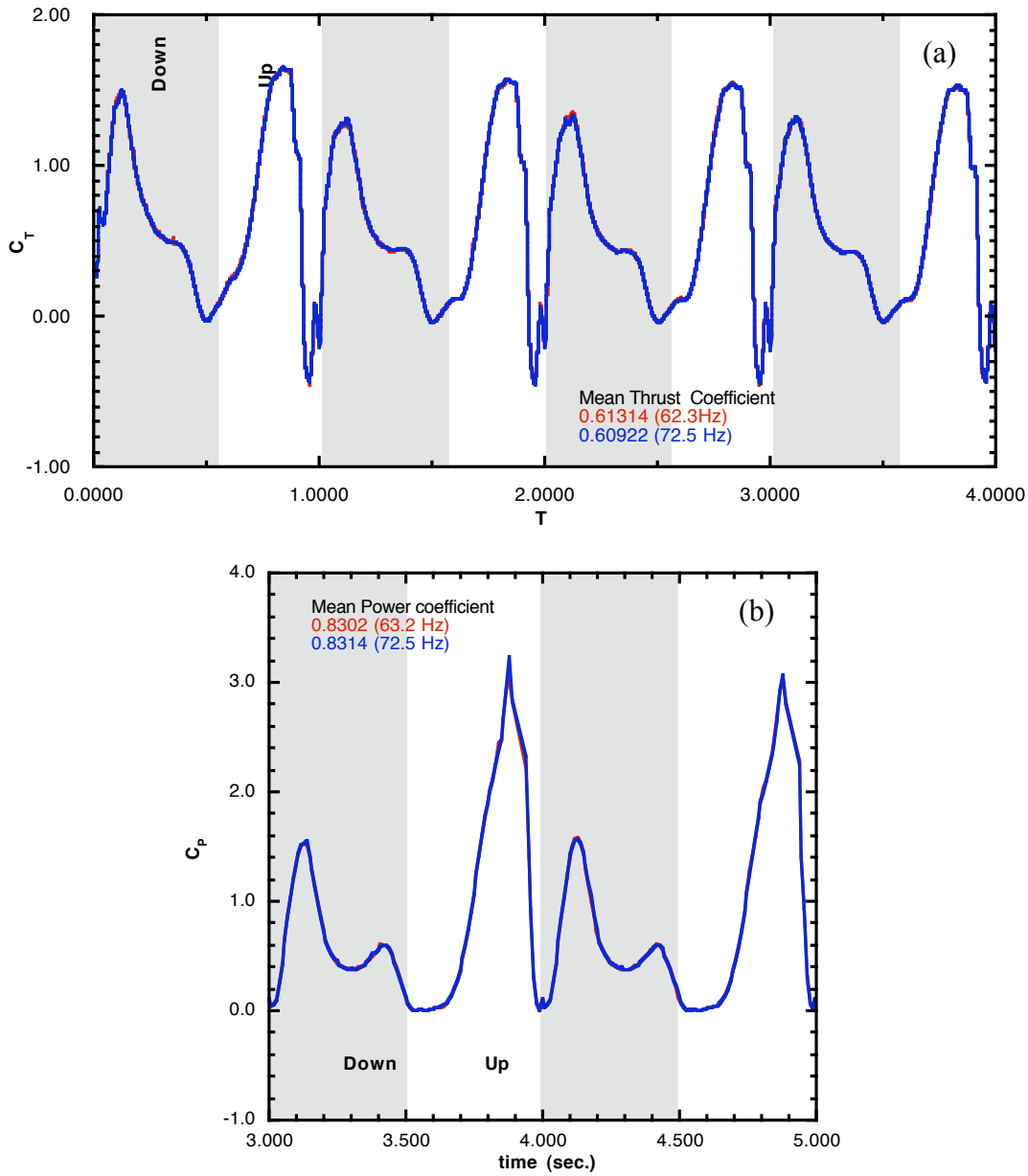


Fig. 22. Variation of Thrust and Power coefficients, run5.04 (red) and run5.04.1 (blue).

5. Aspect Ratio (AR) of the wing:

For this study, wing version d shown in Fig. 6d will be used. The AR will be varied by changing the max chord. The baseline max chord is 1.2cm. This will be changed to 0.9cm and 1.5cm. corresponding to a chord factor of 0.75 and 1.25, respectively. The phase shift for this study is 15.3° and the γ factor is 1.0. The results shown in Fig. 23a suggests that the mean lift varies almost linearly with the chord factor. The thrust coefficients for these three cases also merge almost into a single curve showing the linear behavior with the chord factor.

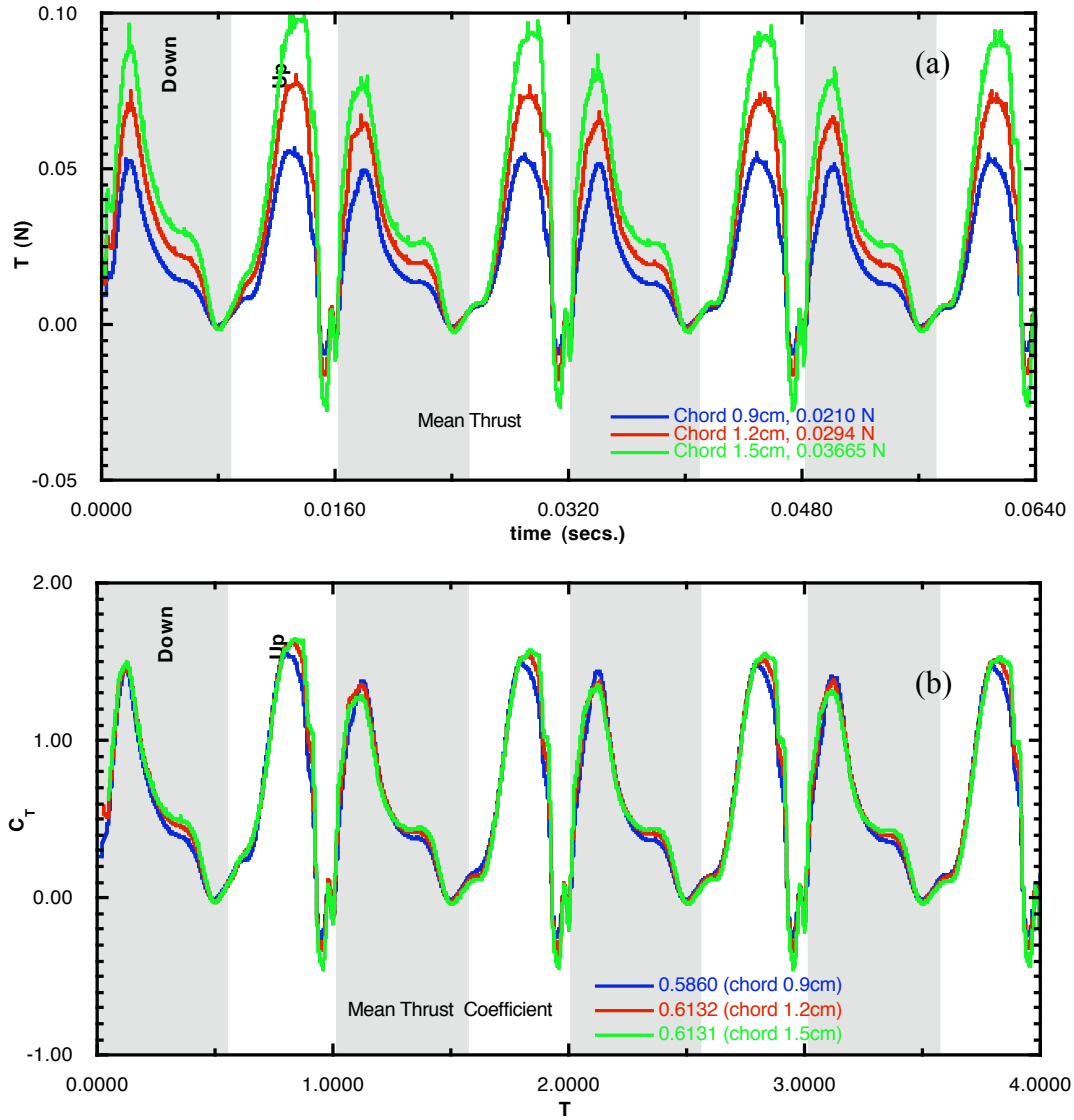


Fig. 23. Effect of chord on the thrust time history, run 2.03 (red), run3.20 (green) and run3.21 (blue).

6. Camber and/or Twist:

For reversing camber, an approach similar to our earlier study of the BITE vehicle [7] is used. The mean camber line would be NACA airfoil camber. The maximum camber location p is fixed to be $0.25c$ and only the max camber y_m , Fig. 24a, is varied. The reversing parameter $A(t)$ follows the rotation angle profile of the Robofly experiment, shown in Fig. 1b. The wing shape is prescribed throughout the cycle at several control points at the leading edge, trailing edge and a 0.75 span of the wing from the root location as shown in Fig. 24b.

$$\begin{aligned}
y_c &= \frac{y_m}{p^2} (2px_c - x_c^2), \quad \{0 \leq x_c \leq p\} \\
&= \frac{y_m}{(1-p)^2} (1 - 2p + 2px_c - x_c^2), \quad \{p \leq x_c \leq 1\}
\end{aligned}
\tag{5a-c}$$

$$y(t) = A(t) \cdot y_c \cdot C(z)$$

$$A(t) = \frac{\gamma_{robotfly}(t)}{0.5(\max(\gamma_{robotfly}(t)) - \min(\gamma_{robotfly}(t)))}$$

Similar reversing function can be used for twist with θ_0 as the free parameter where b is the maximum span of the wing and z is the spanwise location.

$$\theta(z, t) = A(t) \ 2\theta_0 z / b \tag{6}$$

For the case with the γ factor of 1.125, and phase shift of 7.65° , a maximum camber of 10% chord produced a higher mean thrust of 0.038 N compared to the rigid wing which produced approximately 0.0339N, as shown in Fig. 25.

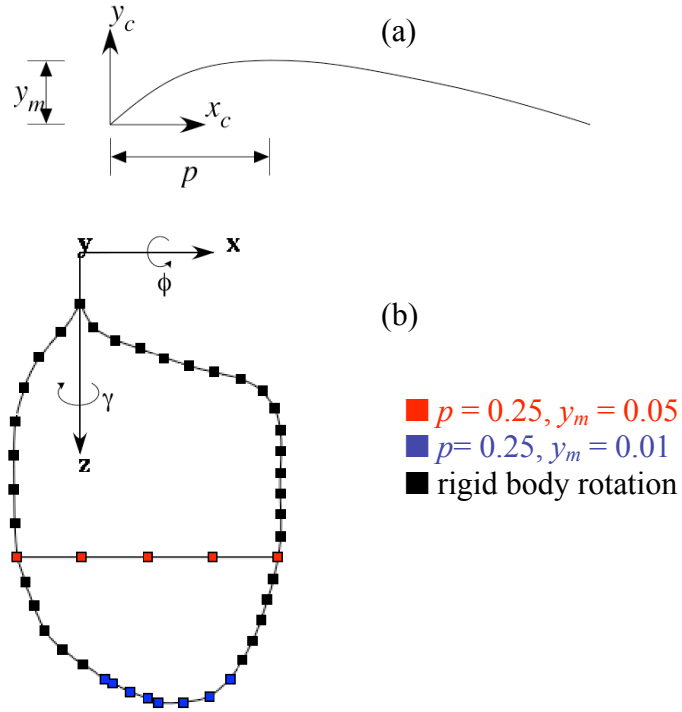


Fig. 24. Prescribing reversing camber kinematics, (a) wing cross section and (b) control points.

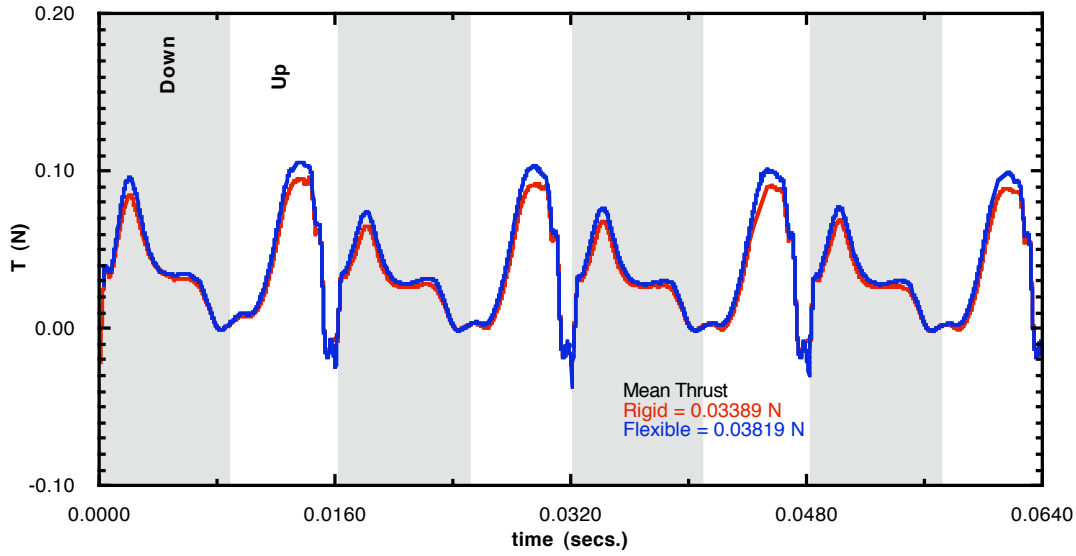


Fig. 25. Effect of reversing camber on the thrust production.

7. Optimization using CFD and Design of Experiments:

For the optimization of the various parameters that control the kinematics of the wing, the kinematics obtained from the experimental observation was used as a baseline. We then varied the other parameters using scaling factors from the baseline kinematics, such as the wing stroke amplitude, ϕ_{fac} , the wing rotation angle or mid-stroke angle of attack, γ_{fac} , the phasing between the wing rotation and stroke reversal, β , and the maximum chord length and the maximum camber at $1/4$ chord location, y_m .

During the initial stages of the optimization study, it was found that the thrust generated increases as the stroke amplitude was increased from the baseline value to 151.7° which was deemed the maximum feasible for the current mechanism. This value corresponds to a ϕ_{fac} of 1.45 and was fixed for the remainder of the simulations. Next, from our frequency scaling computational experiments, it was found that the thrust produced T , scales proportional to f^2 and the aerodynamic power input, P_{aero} , scales proportional to f^3 . Hence, the flapping frequency was fixed at the baseline value of 62.3 Hz. The maximum thrust of 0.0396 N was obtained, run 5.10, with a $\gamma_{fac} = 1.05925$, $\beta = 22.95^\circ$ and $y_m = 0.1$. The figure of merit at this condition was only 18%.

The objective of the optimization is to maximize the figure of merit (FOM) while producing a 10 gf of lift. In order to compare FOMs between simulations, first the frequency, f_{10} , that would produce 10 gf of lift was found using the computed thrust T and the scaling laws for the frequency. Next, the aerodynamic power P_{aero} is scaled to $P_{aero,constrained}$ which is the power required to produce 10 gf of lift. Then, the FOM is obtained from this power and the ideal induced power from an equivalent actuator disk. This is shown in the following equation:

$$\begin{aligned}
f_{10} &= f \sqrt{mg/2T} \\
P_{aero,constrained} &= 2P_{aero} (f_{10}/f)^3 \\
FOM_{hover} &= P_{induced} / P_{aero,constrained} \\
P_{induced} &= \frac{(mg)^{3/2}}{(2\rho A_{swept})^{1/2}}
\end{aligned} \tag{7}$$

where m is the mass of the vehicle ($= 0.01$ kg), $g = 9.8$ m/s², ρ is the density of air ($= 1.2$ kg/m³) and A_{swept} is the area swept by the wing depending on the stroke amplitude.

The set of parameters for each computational simulation was chosen using statistical Design of Computer Experiments [8] method to find the optimal configuration while minimizing the number of simulations. From the computational experiments, it was found that the near optimal set of kinematics parameters is $\gamma_{fac} = 1.25$, $\beta = -15.3^\circ$ and $y_m = 0.04$. From the computational results varying the set of the three control parameters and using the design of experiments, it was found that the maximum FOM can be obtained at $\gamma_{fac} = 1.256$, $\beta = -11.02^\circ$ and $y_m = 0.0455$, and the maximum FOM was 36%. Figure 26 shows the contours of FOM at 3 different camber depths. The optimal design point is shown by the star in Fig. 24b, for convenience, although it occurs on a different plane in the 3-parameter search space.

For the near optimal configuration, the FOM_{hover} was found to be 34.5%. For this case, the mean thrust generated by one wing is 0.0241 N and the P_{aero} is 0.1649 W. The thrust and power time histories are shown in Fig. 27 a and b, respectively. Figure 27a also shows that a rigid wing ($y_m = 0.0$), produces a reduced mean thrust of 0.02196 N yielding an FOM of 29.4%. Figure 28 shows the pressure distribution on the top and bottom surfaces of the wing corresponding to the instant, $t = 0.0$ at which maximum thrust is obtained. It is clear that lower suction peaks and larger high pressure peaks on the bottom and top surfaces, respectively, are attained in the

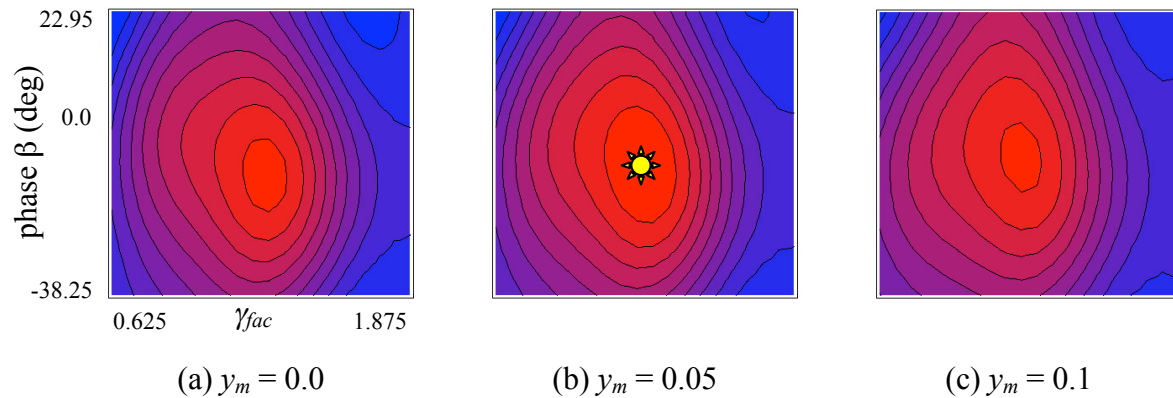


Fig. 26. Contours of FOM using Design of Experiments to find optimal combinations of design parameters of the kinematics of the flapping wing.

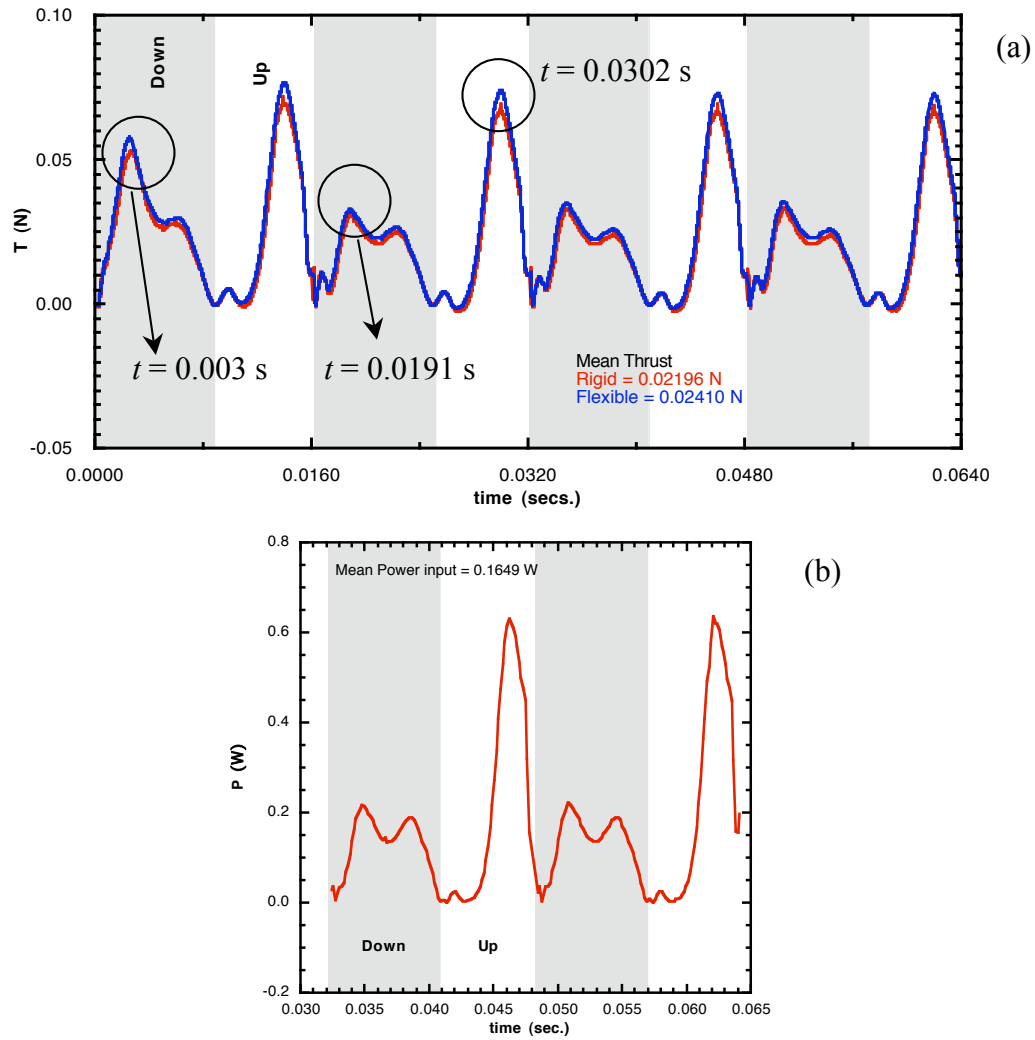


Fig. 27. Variation of (a) thrust and (b) aerodynamic power for the near optimal configuration, run6.05 (red) and run6.06 (blue).

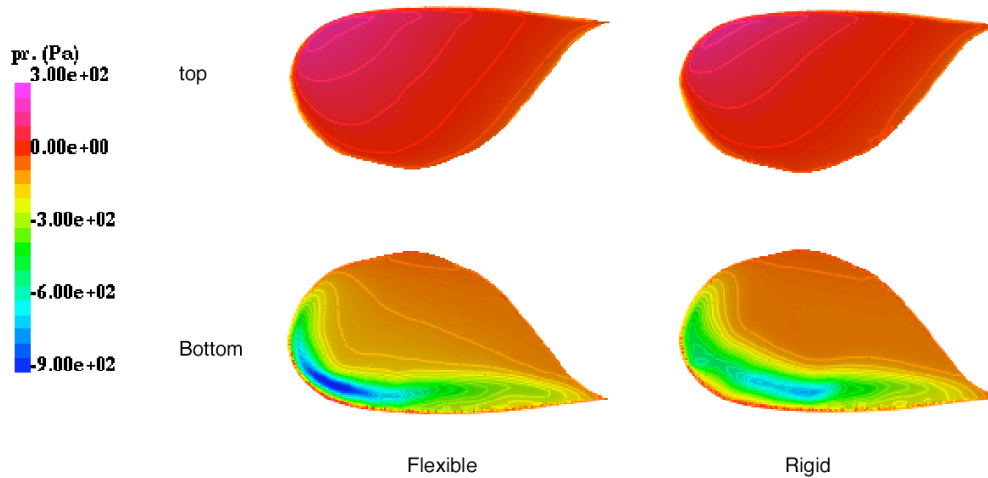


Fig. 28. Surface pressure distribution on the rigid and flexible wings at $t = 0.0302$ s, during the upstroke.

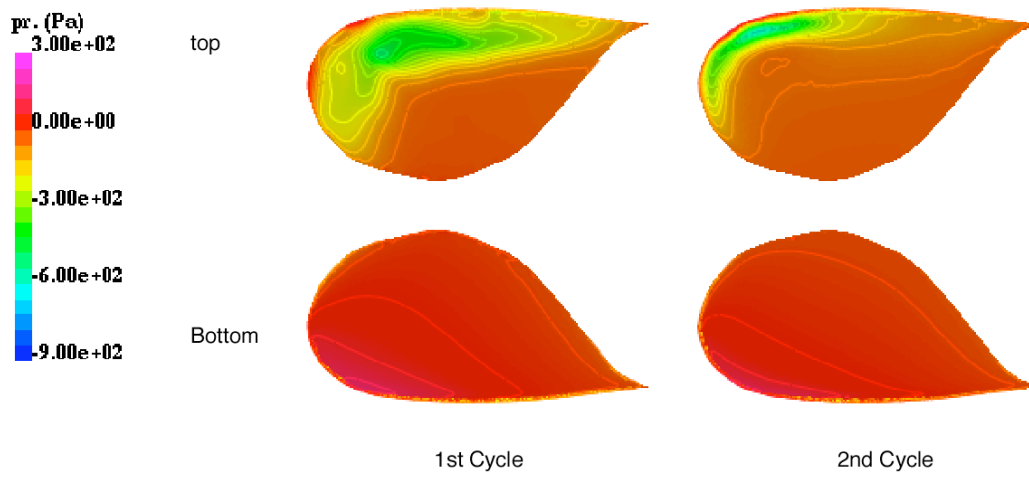


Fig. 29. Surface pressure distribution during the first and second flapping cycles at the instant of maximum thrust during the down stroke, showing the effect of wake capture.

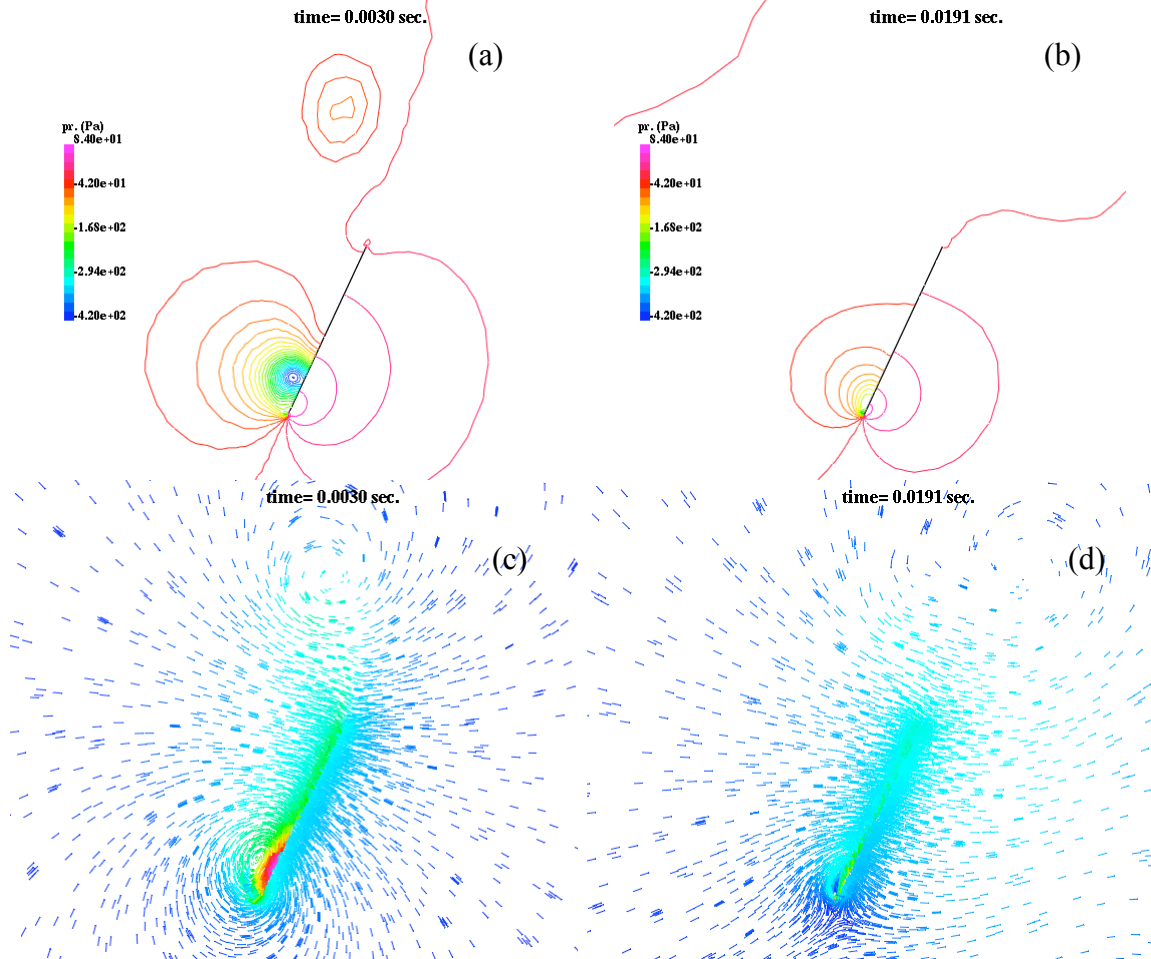


Fig. 30. Pressure and velocity vectors on a plane cut $z = 3.5$ cm.

flexible wing case compared to the rigid case, resulting in a larger lift force. Also, it is interesting to note that the peak thrust during the first cycle of flapping, $t = 0.003\text{s}$ is larger compared to the peaks in the successive cycles. This is mainly due to the influence of the downwash in the wake which reduces the effective angle of attack, Fig. 29. This effect is also observed in experiments by Birch and Dickinson [9]. Figure 30 a-d show the pressure and velocity vectors on a plane 3.5cm from the symmetry plane at these instants during the first two flapping cycles. It is clear that the leading edge vortex during the first cycle is much stronger compared to the second cycle. Figure 31 show the particles traces and the presence of the leading edge vortex which merge with the wing tip vortex close to the instant when the maximum thrust is attained during the upstroke.

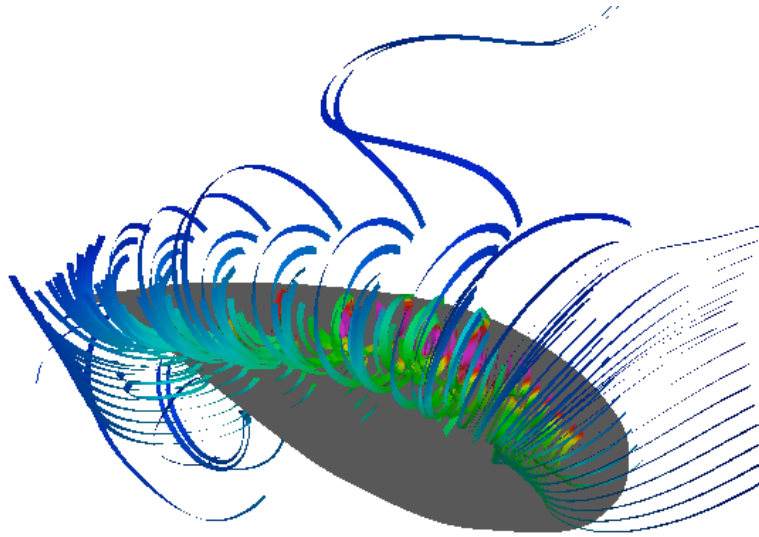


Fig. 31. Particle traces at $t = 0.0298\text{ s}$.

8. Effect of Planform:

Several plan forms of the wing have been tested both experimentally and in computational studies, as shown in Fig. 32. The characteristic dimension that distinguishes these planforms is the mean chord of the wing which can be defined as

$$\bar{C} = \frac{A_w}{L_{span}} \quad (8)$$

where A_w is the area of the wing and L_{span} is the span of the wing. In all our studies, the span of the wing is maintained to be 3.75cm.

The initial configuration of the wing Fig. 32b used with the first mechanism built is found to be restrictive in the stroke amplitude and therefore, the trailing edge portion near the root was modified. Version 2.0c, Fig. 32c, is further modified to remove the leading edge portion of the wing ahead of the wing rotation axis to yield better turning characteristics during stroke reversal, resulting in wing version d, Fig. 32d. The optimization study for the kinematics is performed with the version d of the wing and the near optimal kinematics is used to evaluate the performance of the two paddle-shaped wings Fig. 32e and f. Finally, the planform of the fruitfly

wing is scaled to have the 3.75cm wing span and is used to compare the performance of the version d of the wing using the kinematics obtained from the Robofly experiments.

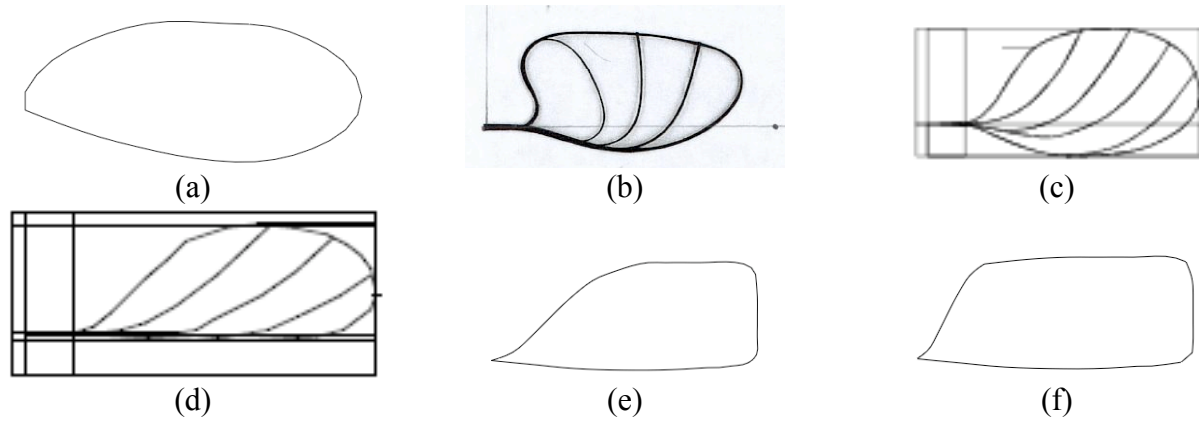


Fig. 32. Various planforms of wings tested in experiments and computations.

(a) fruitfly *Drosophila*, $\bar{C} = 0.8524$ cm, (b) version 1.0, $\bar{C} = 1.4291$ cm, (c) version 2.0, $\bar{C} = 1.509$ cm, (d) version d, $\bar{C} = 0.6944$ cm, (e) paddle 1, $\bar{C} = 0.7619$ cm and (f) paddle 2, $\bar{C} = 0.8755$ cm.

With the near optimal kinematics described in the previous section, the wing planform was changed to the paddle 2, Fig. 32f. This resulted in a mean thrust of 0.03048 N, Fig. 33a, and a mean aerodynamic power of 0.23 W, Fig. 33b, yielding a slightly improved FOM of 35.15%.

Propeller vs Flapping

In order to study the differences between the propulsive efficiency of a propeller to a flapping wing, first a propeller was designed by Steve Morris to produce 10g of thrust. This propeller has a high twist from the root to the tip. The shape of the propeller is given as

$$c = 0.75 - z/3 \text{ (in)} \\ \theta_{prop}(z) = \tan^{-1}\left(\frac{0.23873}{z}\right) - 3.0 \text{ (deg)}, \quad 0 \leq z \leq 1.5", \quad (9)$$

where c is the chord, z is the radius of the spanwise location and θ_{prop} is the twist angle from the plane of rotation. The maximum camber at each spanwise section is set to 4% of the chord and at 25% of the chord. The resulting geometry is shown in Fig. 34.

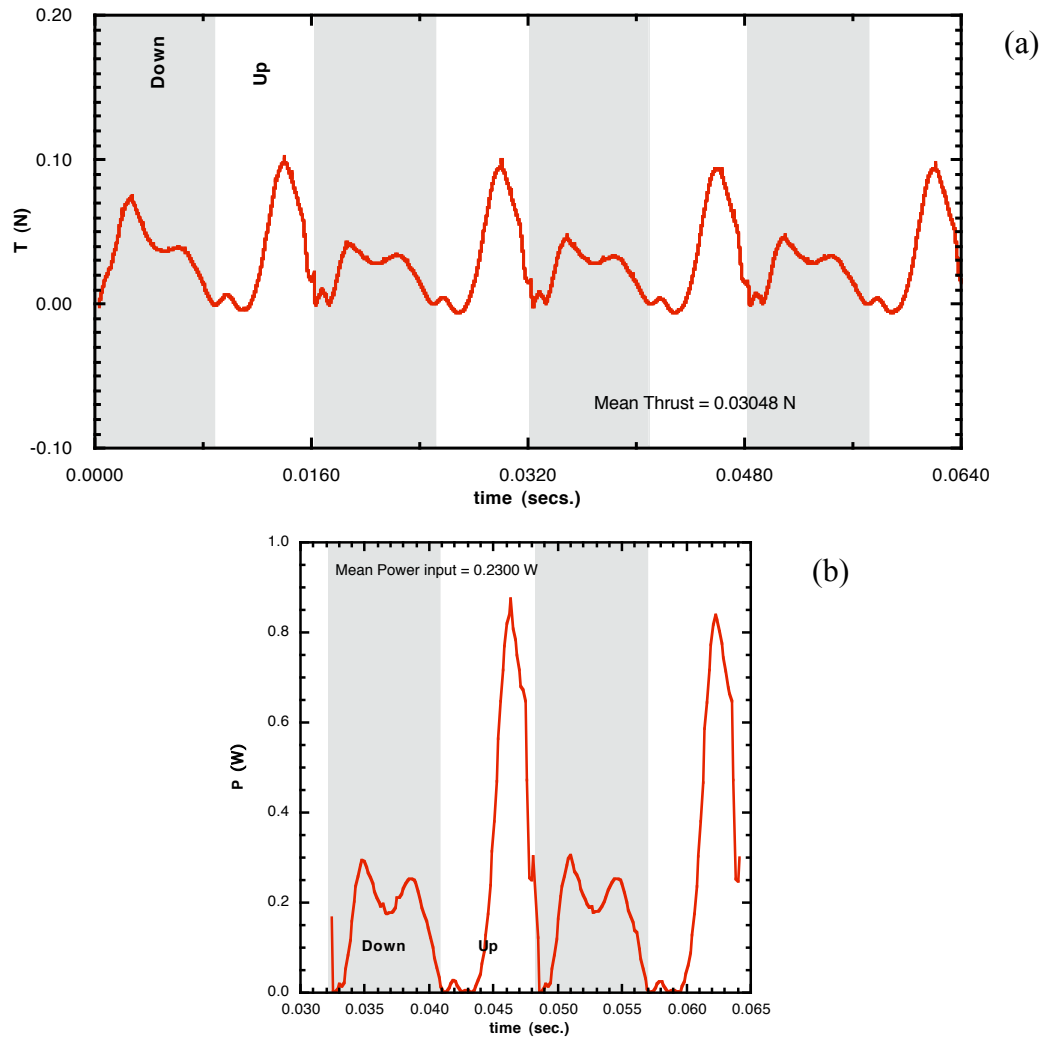


Fig. 33. Thrust and aerodynamic power variation at the near optimal kinematics using paddle 2 planform, run 7.09

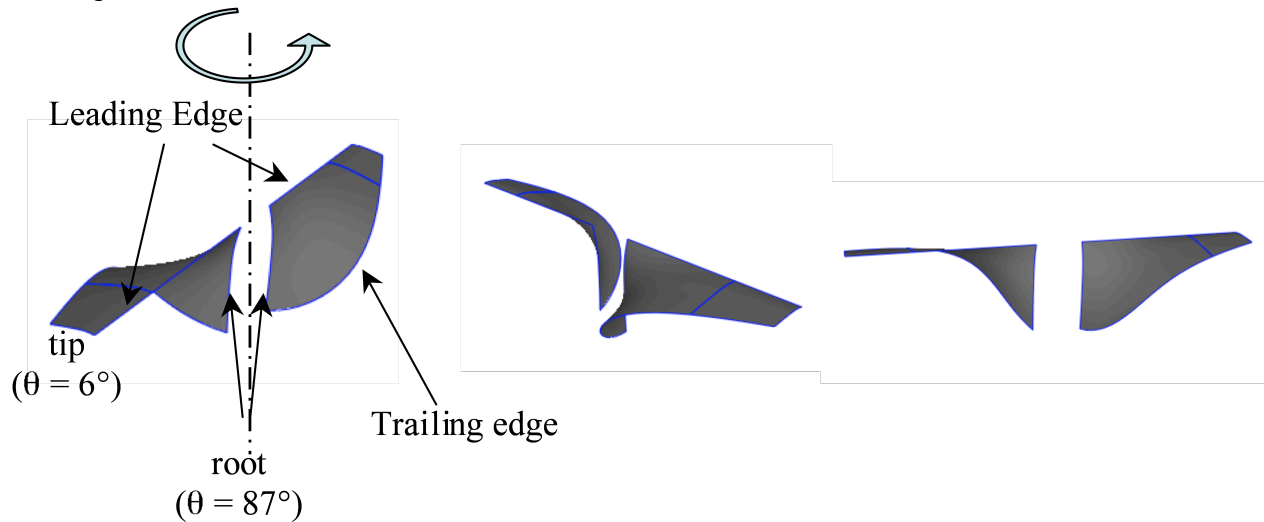


Fig. 34. Three views of the geometry of the rotating propeller.

Computations were performed for this propeller rotating at 8750 rpm in a rotating frame of reference. The resultant thrust generated by the two blades is 0.10817 N and the aerodynamic power input to the propeller is 0.6405 W, resulting in a FOM of approximately 54%. The pressure and the magnitude of velocity on the top and bottom surfaces of the propeller blade are shown in Fig. 35. The same configuration was computed in a stationary frame of reference with the propeller blades modeled as moving bodies at the specified rpm. Figure 36 shows the time history of the thrust and aerodynamic power input for this propeller. The mean thrust for the 2 bladed propeller is 0.16761 N and the mean power input is 1.0053 W, resulting in a FOM of 66.3%. Again, this is similar to the results obtained with the helicopter blade design code of Steve Morris.

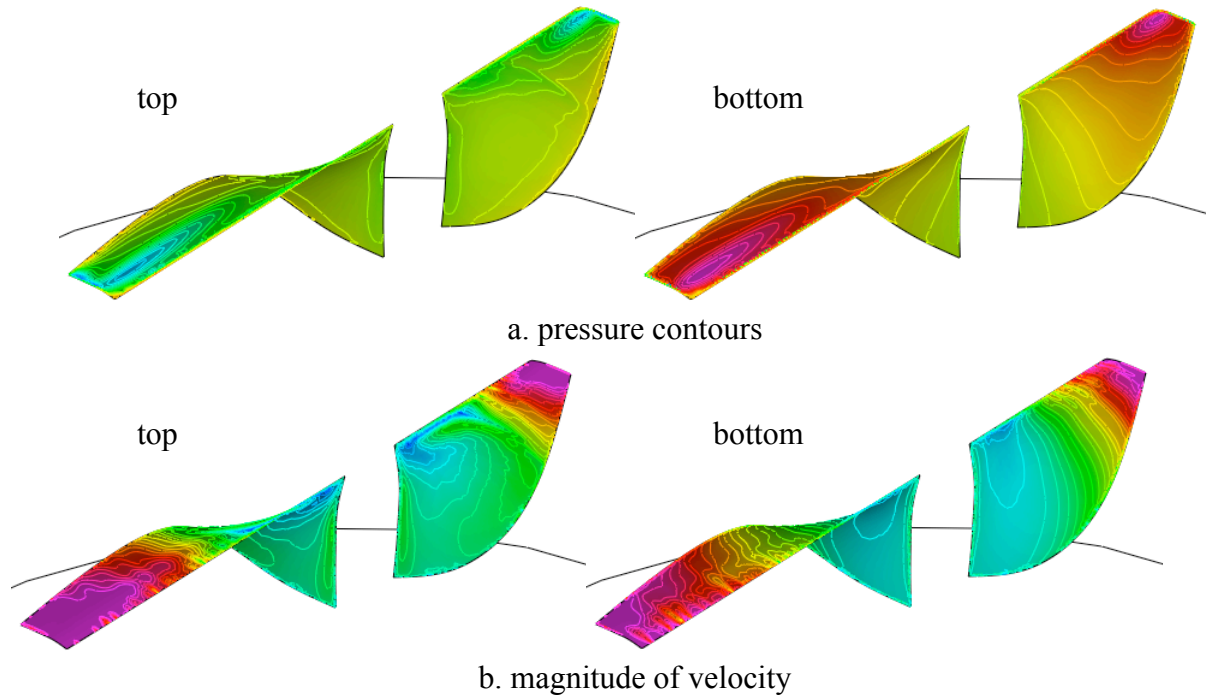


Fig. 35. Surface pressure and velocity distribution on the propeller blades rotating at 8750 rpm.

In order to study the effect of viscosity, a viscous computation was carried out at a $Re = 34,000$ based on the mean tip speed of 34.36m/s and the mean chord of 1.479cm. Figure 37 shows the time history of thrust and the aerodynamic power input to the propeller. The overall figure of merit for this case is reduced to 59.6% from the inviscid value of 66.3%.

Propeller as a flapper

The propeller blade described above was used as a flapping wing with reversing camber and twist. The robot fly rotation angle profile (Eq. 6c) is used to provide the reversing camber and twist.

$$\theta(z,t) = A(t) \theta_{prop}(z) \quad (10)$$

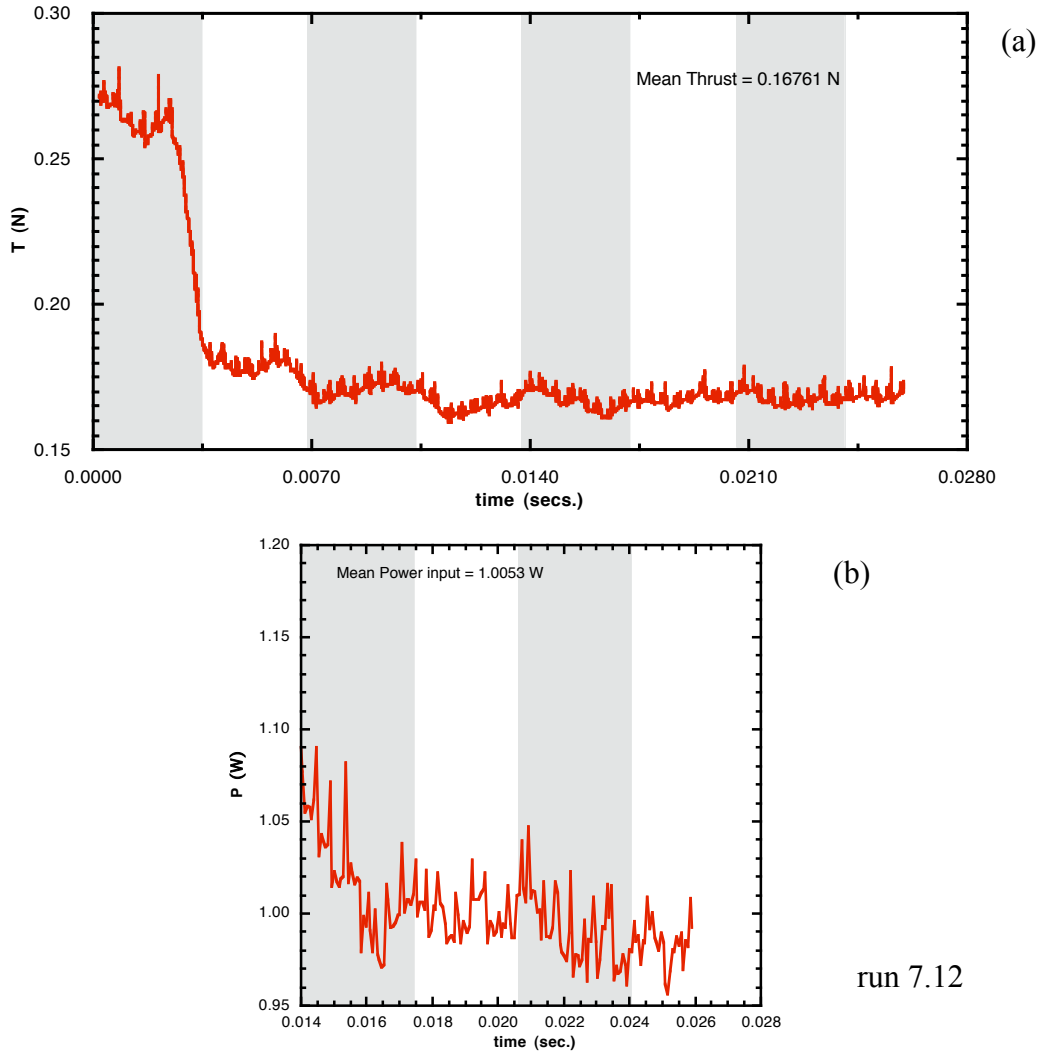


Fig. 36. Thrust and aerodynamic power variation in a propeller rotating at 8750 rpm.

The kinematics for the flapping propeller blade is shown in Fig. 38. For this blade flapping at 145.8333 Hz, the resultant time history, Fig. 39a, shows that the mean thrust produced by one wing is 0.171 N and the mean aerodynamic power input to the blade is 6.2776 W, Fig. 39b, resulting in a FOM of approximately 15.5%. Although the mean thrust produced by the flapping propeller blade is almost twice that of the rotating propeller ($= 0.0838$ N), the mean power required per cycle is nearly 12 times that of the propeller ($= 0.5027$ W) per blade, resulting in a reduced FOM. From the frequency scaling, we can obtain a thrust of 10 gf with two wings flapping at 78 Hz. Figure 39a shows that the thrust production is negative just after stroke reversals and from Fig. 39b we can see that the power input reaches a maximum just before stroke reversals. Similar trends are shown in the time history of the coefficient of thrust and drag shown in Fig. 40. The ratio of the thrust and drag coefficients, Fig. 41, show that after stroke reversals the ratio reaches a large negative values. At these instants the thrust produced is negative. This is largely due to the specified kinematics, which shows a large acceleration of the trailing edge points in the y -direction, Fig. 42. This produces a high pressure on the top surface of the blade and a lower pressure on the bottom, resulting in the negative thrust/lift.

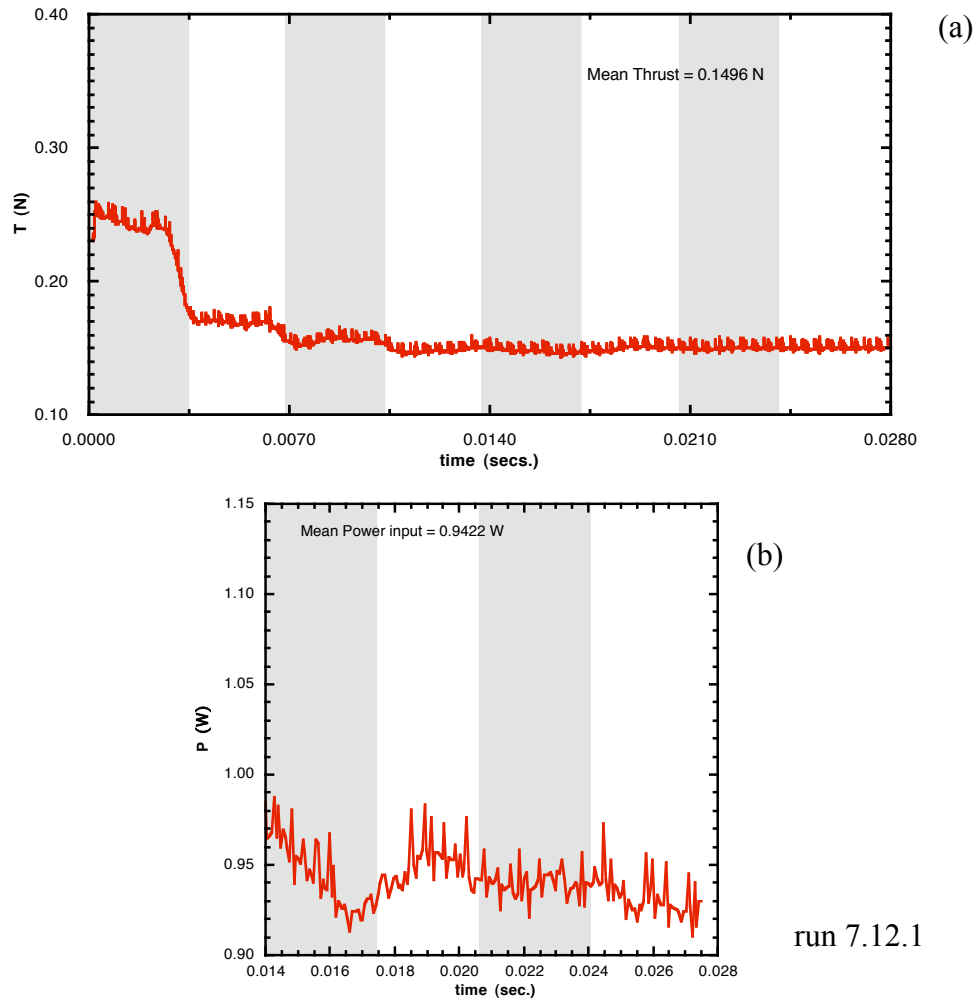


Fig. 37. Thrust and aerodynamic power variation in a propeller rotating at 8750 rpm, $Re = 34,000$.

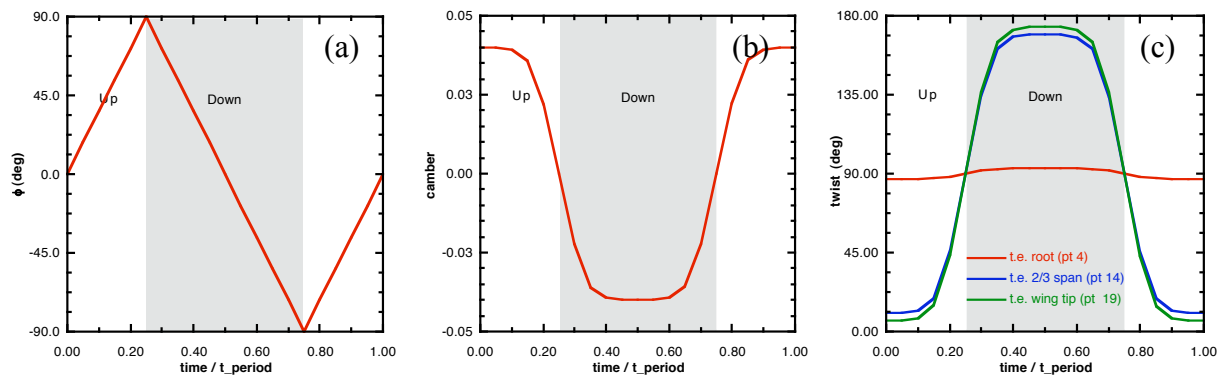


Fig. 38. Kinematics of the flapping propeller, run 7.10.

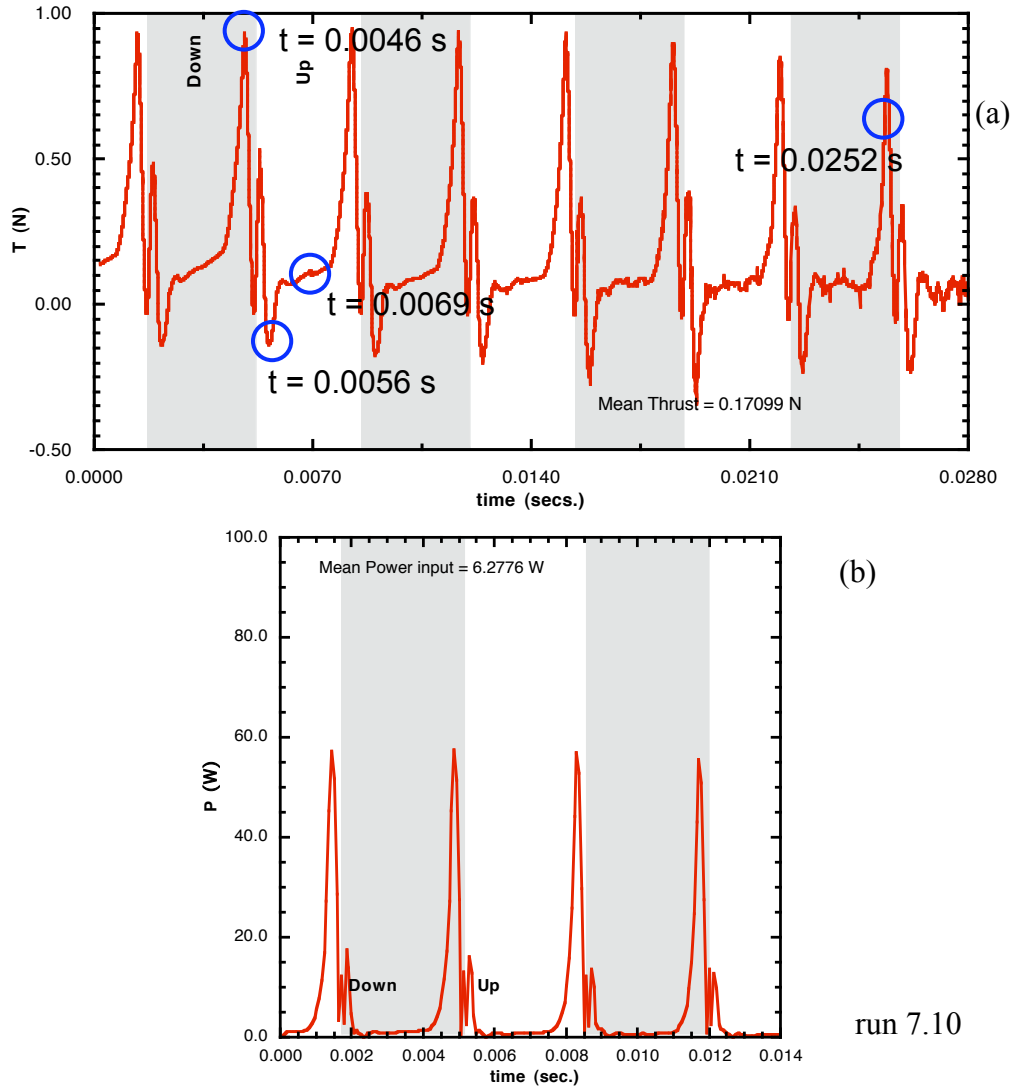


Fig. 39. Thrust production and aerodynamic power input to the flapping blade, $f = 145.8333$ Hz.

The flow around the flapping foil at instants just before and after stroke reversals and in the middle of the upstroke was examined. The pressure and velocity distributions on two spanwise plane cuts were obtained. Figure 43 shows the locations of the plane cuts at $1/3$ and $2/3$ along the span from the root and the rake with respect to the blade. Fig. 44a and b show the pressure distribution and Figs. 44c and d show the magnitude of velocity on these plane cuts at the instant when the thrust generation is maximum right before stroke reversal at $t = 0.0046$ s. It is clear from Fig. 44d and e, that both leading and trailing edge vortices are present. Figure 45 shows the particle traces released from the rake and the presence of the leading edge vortex and the wing tip vortex are seen. The pressure distribution on the top and bottom surfaces of the wing shows high pressure on the bottom, Fig. 45c, and lower pressure on the top, Fig. 45d, leading to a peak thrust force.

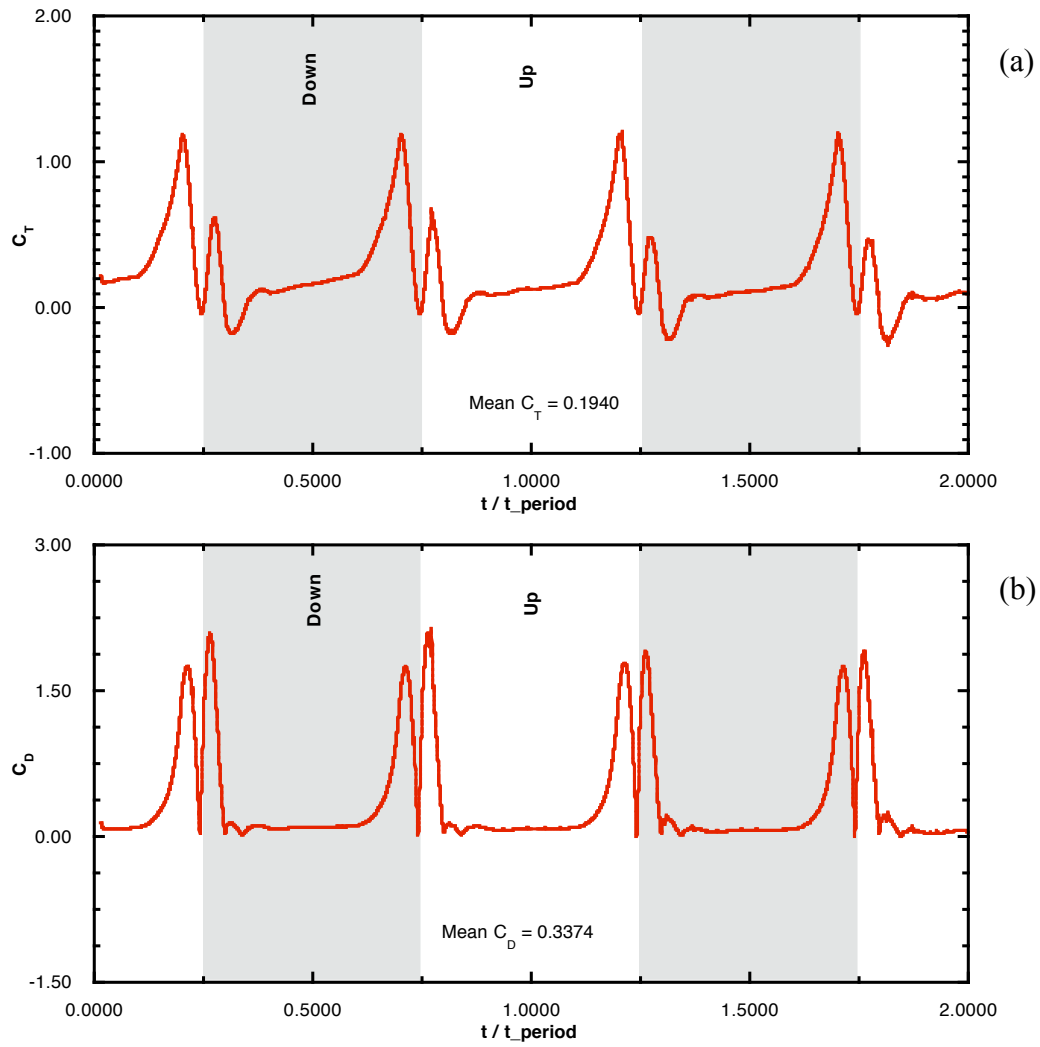
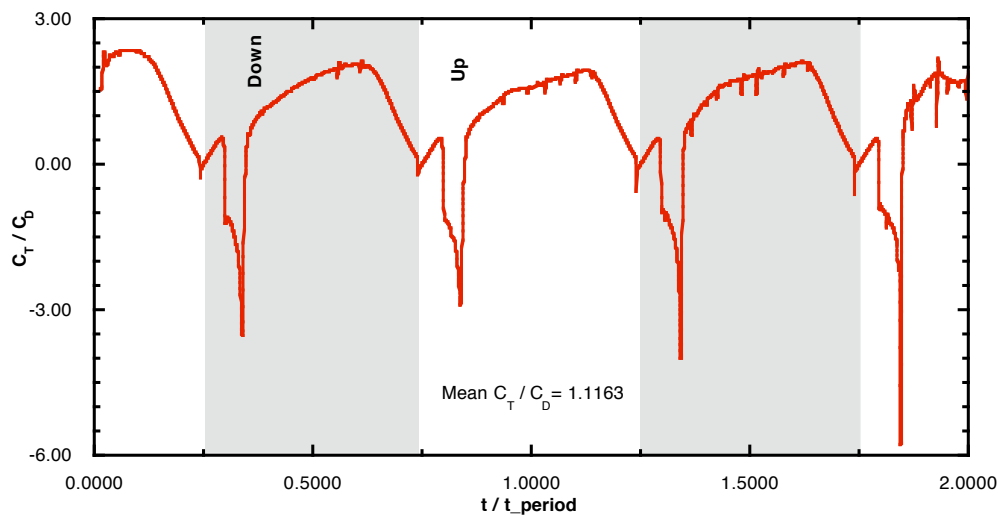


Fig. 40. Time history of the coefficient of thrust and drag.

Fig. 41. Time history of C_T/C_D for the flapping propeller blade.

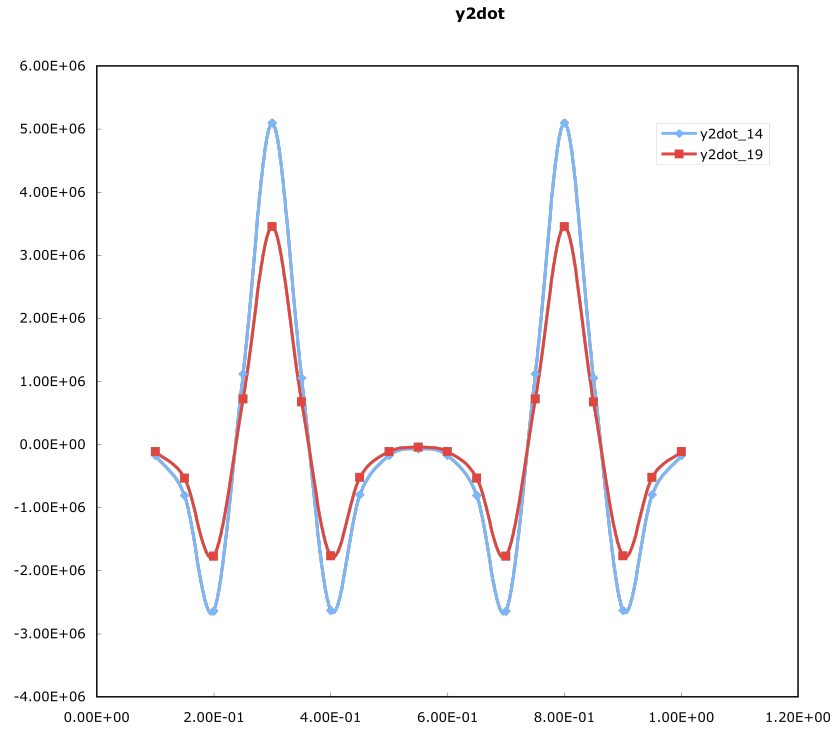


Fig. 42. Vertical acceleration of 2 trailing edge points.

With the flapping frequency reduced to 80Hz, the mean thrust developed by this propeller blade as a flapper is 0.04725N and the mean aerodynamic power is 0.971 W, as shown in Fig. 46a and b, respectively. It is clear that the aerodynamic power peaks near stroke reversals. Therefore, the mean aerodynamic power and the mean thrust generated during the middle 30% of each of the up and down strokes were computed and the resulting FOM is 48%. Hence, the kinematics was modified so that the stroke reversal for twist is achieved faster as shown in Fig. 47. Also for this case, the stroke amplitude was reduced to 160deg and the chord at the root of the blade was reduced by 20%. These modifications were necessary in order to avoid the trailing edges of the blade from colliding into each other during stroke reversals. With this set of kinematics, the mean thrust from the blade flapping at 80.0Hz is 0.0441N and the mean power input is 0.563W, resulting in an overall FOM of nearly 24%; the FOM for the middle 80% of the stroke is 66.7% which matches that obtained from the rotating propeller. The thrust and power time histories for this case are shown in Fig. 48a and b. Attempts to change the plan form of the blade to a rectangular one and modifying the phasing of the twist with respect to stroke reversal by advancing and delaying by 8% of the stroke period did not result in any improvement in the FOM. Finally, the stroke profile was modified from a triangular waveform profile to a smoothed profile that is obtained from the Robofly, as shown in Fig. 49a. The twist and the camber for this case are as shown in Fig. 50b and c. With this modification, the mean thrust over a cycle is 0.03427N and the mean power input is 0.03437 W, yielding an overall FOM of nearly 27%. The corresponding FOM for the middle 60% of the stroke is 57%. The thrust and power time histories for this case are shown in Figs. 50a and b, respectively. Another attempt is made to improve by changing the mid stroke angle of attack at the tip of the blade, see Fig. 34, from 6° to

15°. The mean thrust in this case is 0.04331 N and the mean input power is 0.04758 W, resulting in an overall FOM of 27.6%, but the mid-stroke FOM dropped to 44.5%.

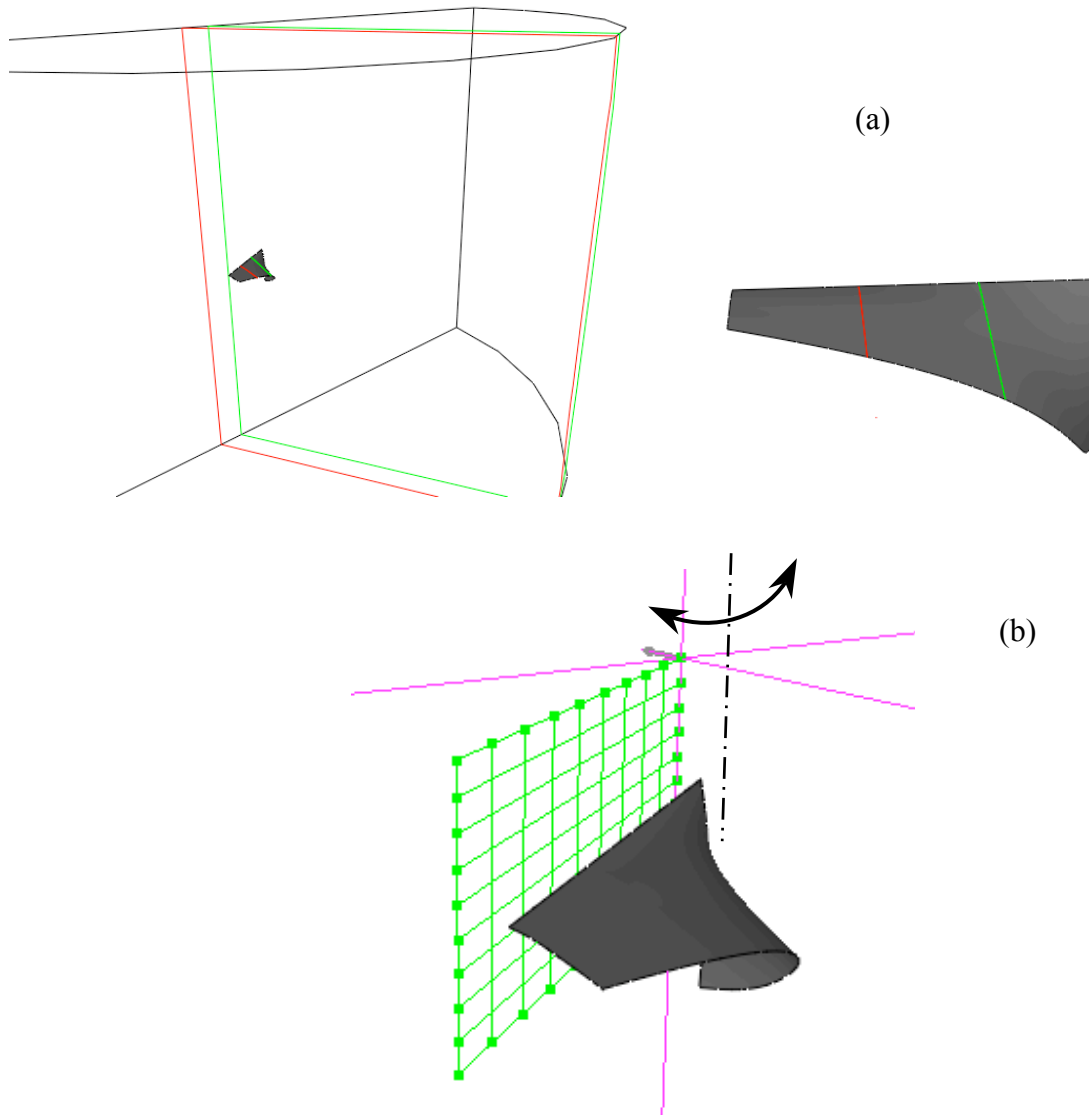


Fig. 43. Plane cuts and particle rake locations for flow visualization.

The effect of viscosity was studied for the flapping propeller case, in order to examine if there is separated flow along the chord during the mid stroke. The kinematics for this case is same as run7.20, shown in Fig. 49. The Reynolds number based on the wing tip velocity and the mean chord of 1.09 cm is 12,200. The mean thrust and power input are shown in Fig. 51. The mean thrust dropped slightly from 0.03029 N and the mean power per cycle also reduced to 0.3139 W, resulting in an FOM of 24.8%; the mid stroke FOM for this case is also slightly reduced to 53.9%.

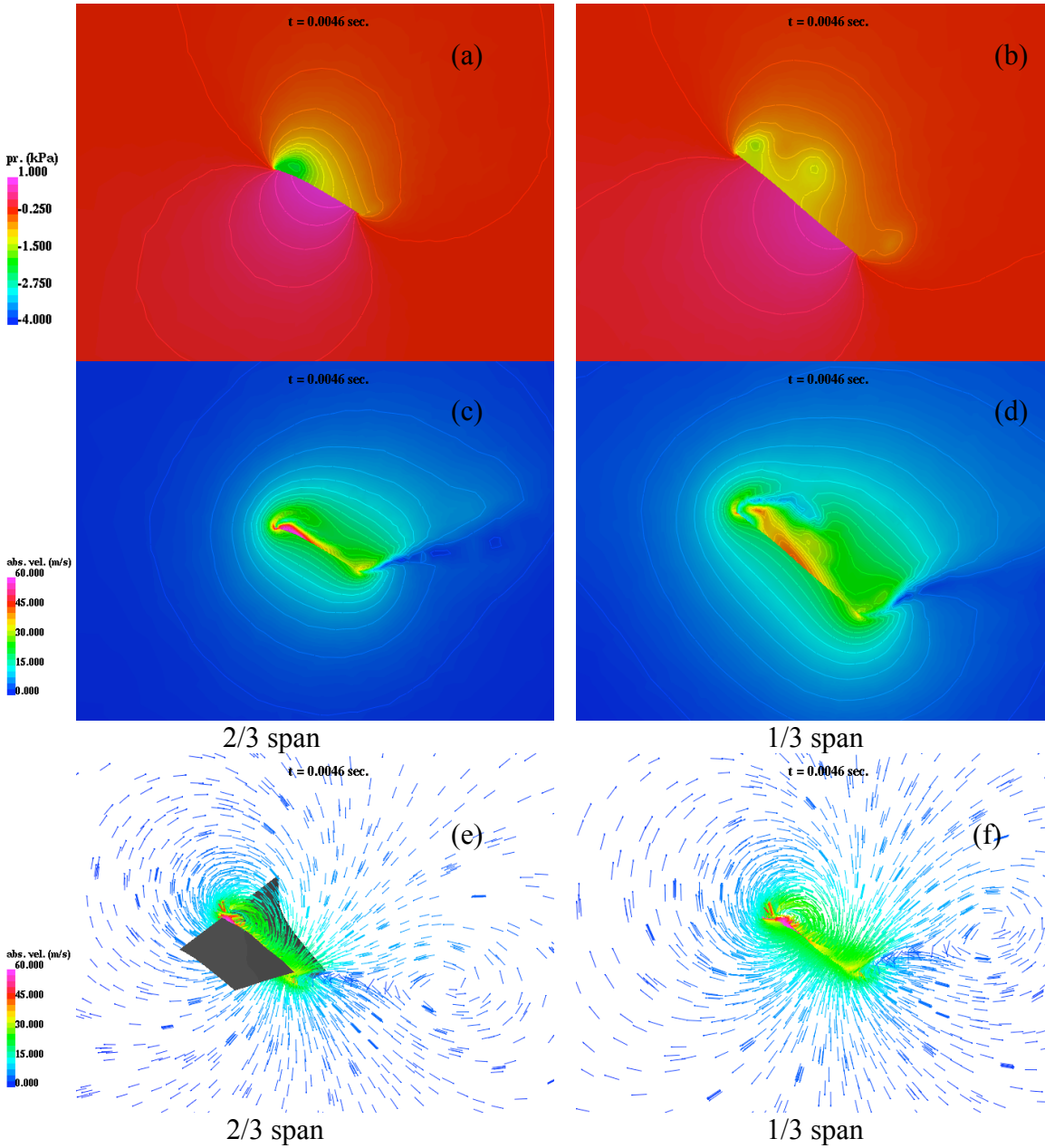


Fig. 44. Pressure, magnitude of velocity and velocity vectors at $t = 0.0046$ secs.

A closer look at the flow shows that near the stroke reversals both leading and trailing edge vortices are being shed at stroke reversals, $t = 0.0134$ s and $t = 0.0196$ s, and during midstroke, $t = 0.0165$ s and $t = 0.0216$ s, only tip and root vortices are present around the blade. These features are shown in the iso-vorticity contours in Fig. 52 a-d. Figure 53 shows the second invariant of the gradient of velocity, a quantity that is a good indicator of the vortex core [10]. From this figure also, we see the leading and trailing edge vortices and the tip vortex.

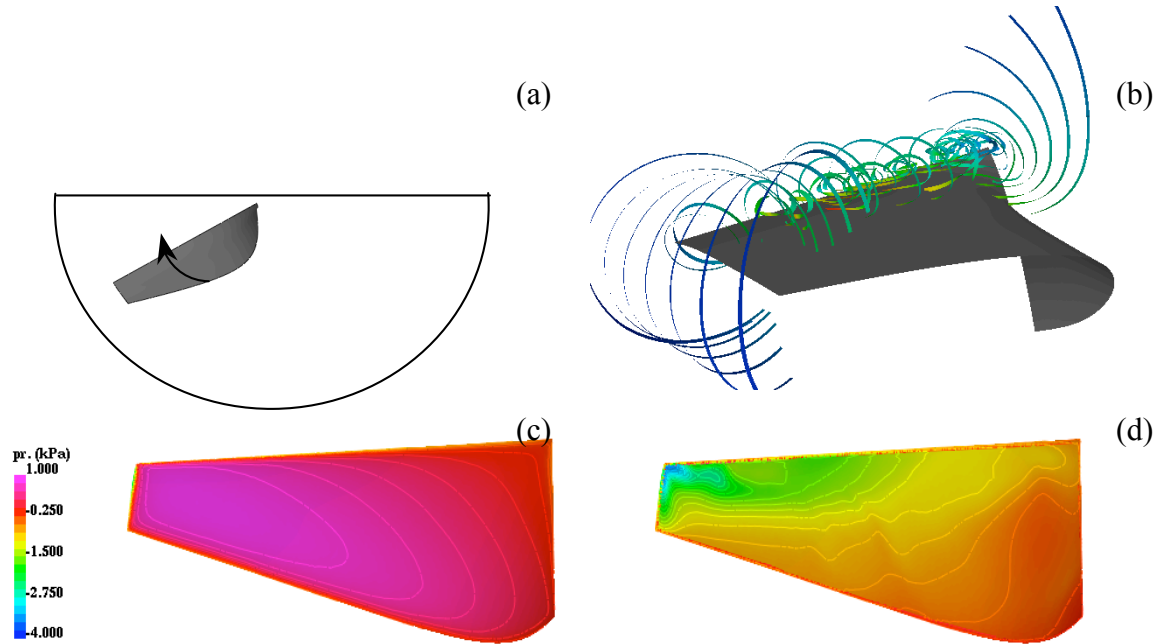


Fig. 45. Flow past a flapping propeller blade at $t = 0.0046$ secs, (a) position of the blade during the downstroke, (b) particle traces near the leading edge, surface pressure distribution on (c) top and (d) bottom of the blade.

Summary and Future Work

Computational fluid dynamics studies of the 3-D unsteady flow past a flapping wing were conducted for the development of a NAV. The focus of this computational study was to gain insight to the design of high performance flapping wings. The primary focus of the computational study was on the aerodynamic performance of the wings in order to obtain a near optimal kinematics of the wing while the NAV is in a hover mode. CFD simulations coupled with Design of Experiments were conducted to arrive at the near optimal kinematics for the NAV design. Several parametric studies were performed varying the stroke angle, the wing rotation angle or the angle of attack, the phasing between these two rotations, the flapping frequency, the aspect ratio of the wing and the planform. It was found that the near optimal kinematics yielded an efficiency or a figure of merit in hover of 35%. In comparison, from our previous work on hovering fruitflies, the FOM in hover is only around 20%. The lower efficiency in flapping propulsion may be due to the losses generated at stroke reversals.

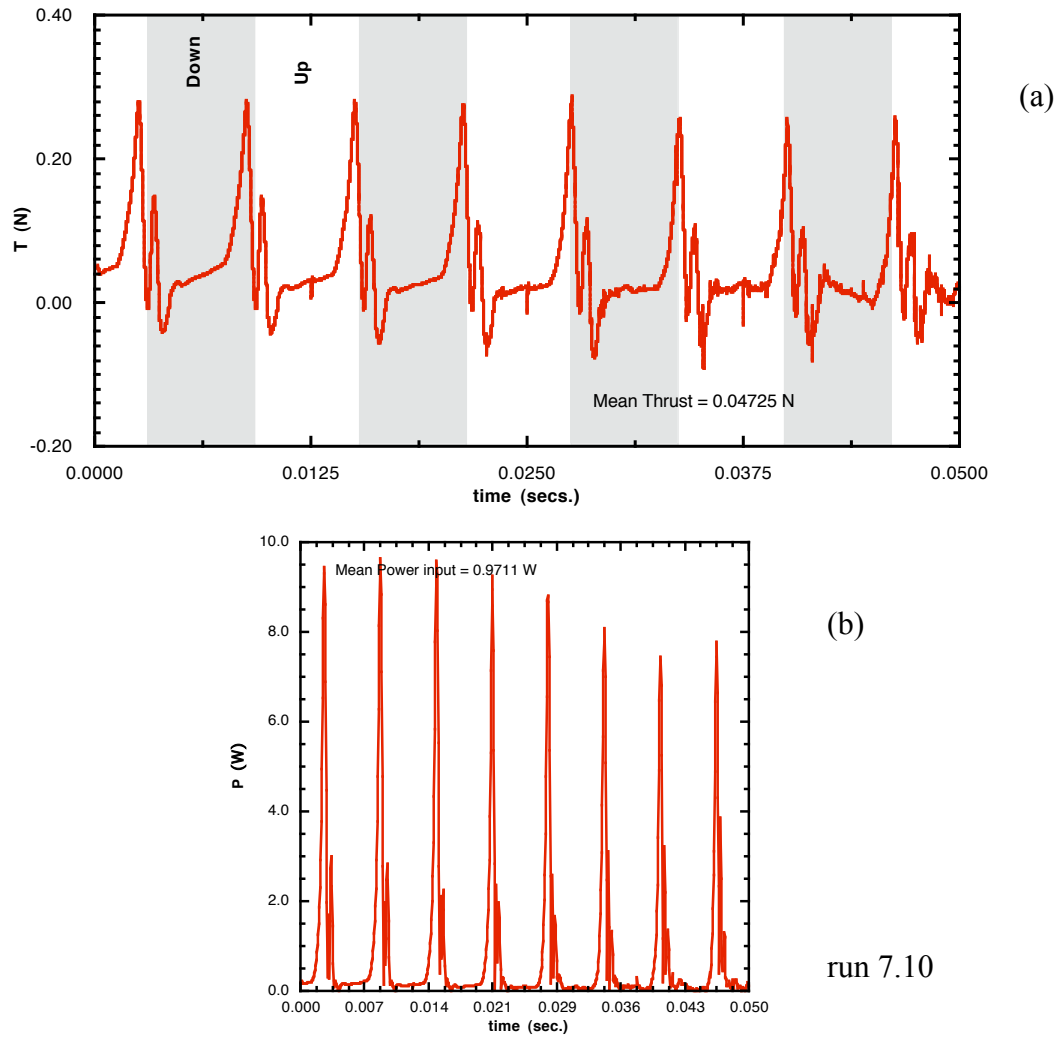


Fig. 46. Thrust production and aerodynamic power input to the flapping blade, $f = 80.0\text{Hz}$.

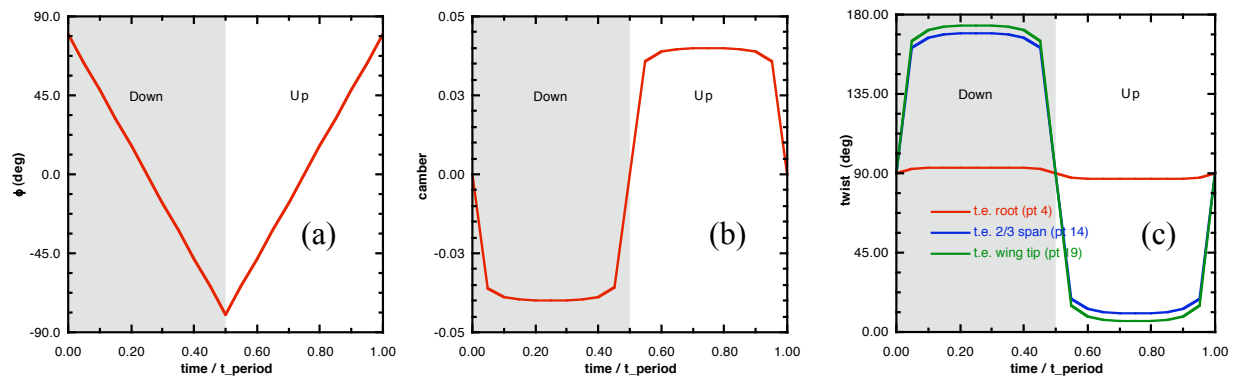


Fig. 47. Improved reversing twist kinematics for a flapping propeller blade, run 7.14.

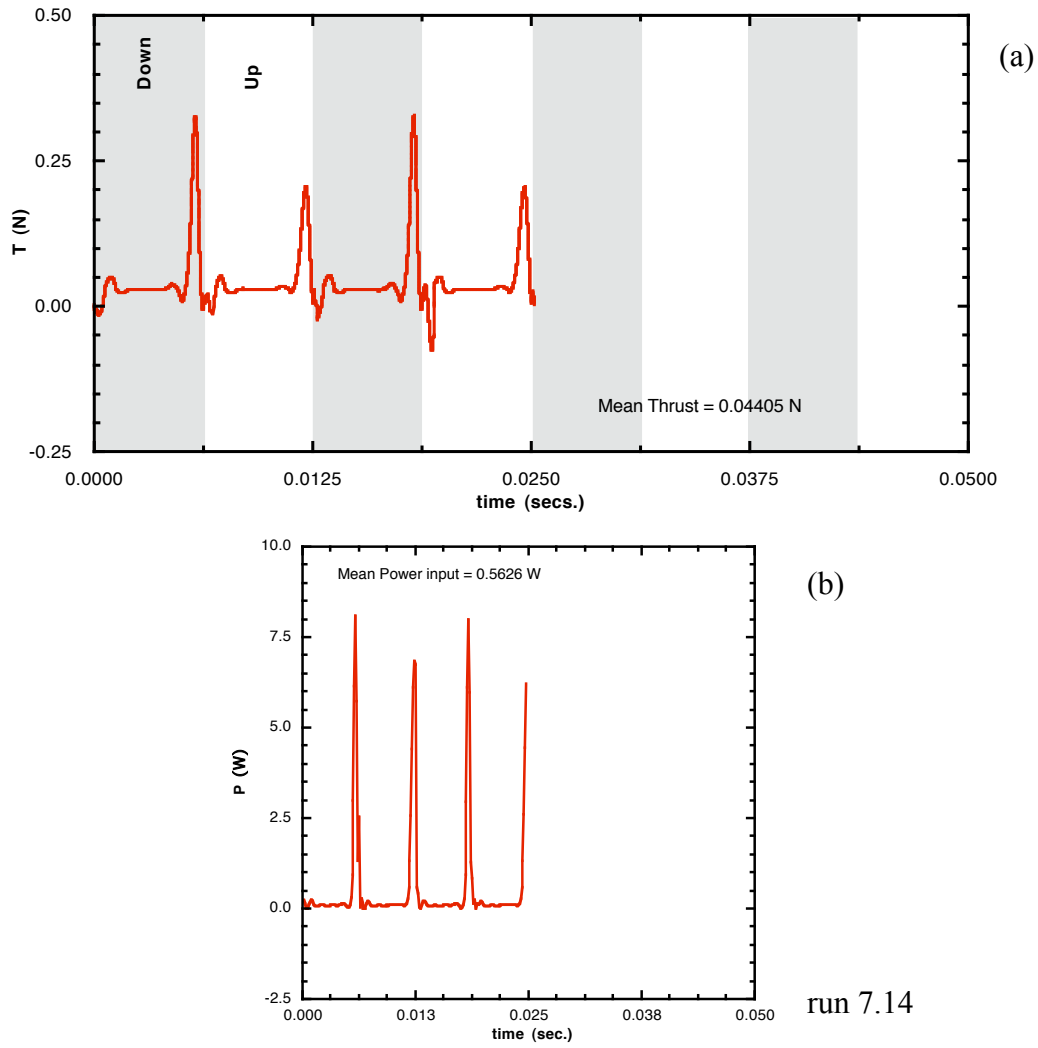


Fig. 48. Thrust production and aerodynamic power input to the flapping blade, $f = 80.0\text{Hz}$.

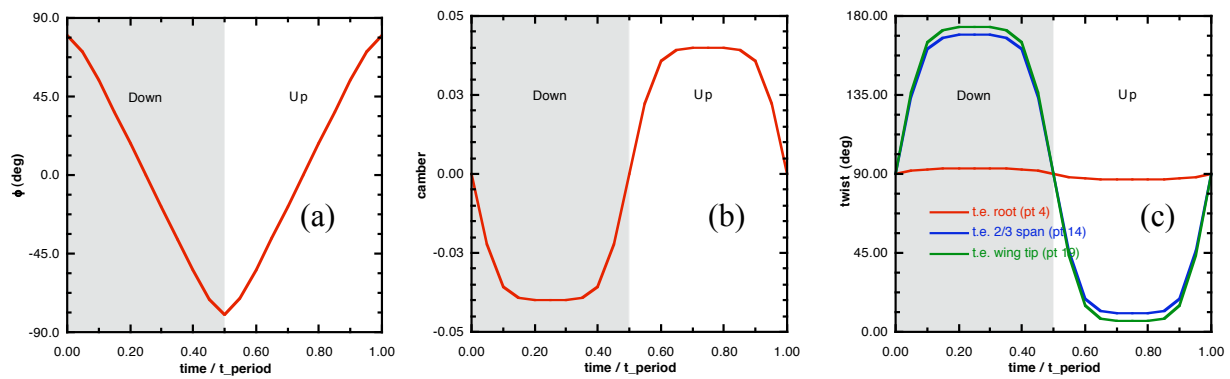


Fig. 49. Modified stroke angle profile for the flapping propeller blade, run 7.20.

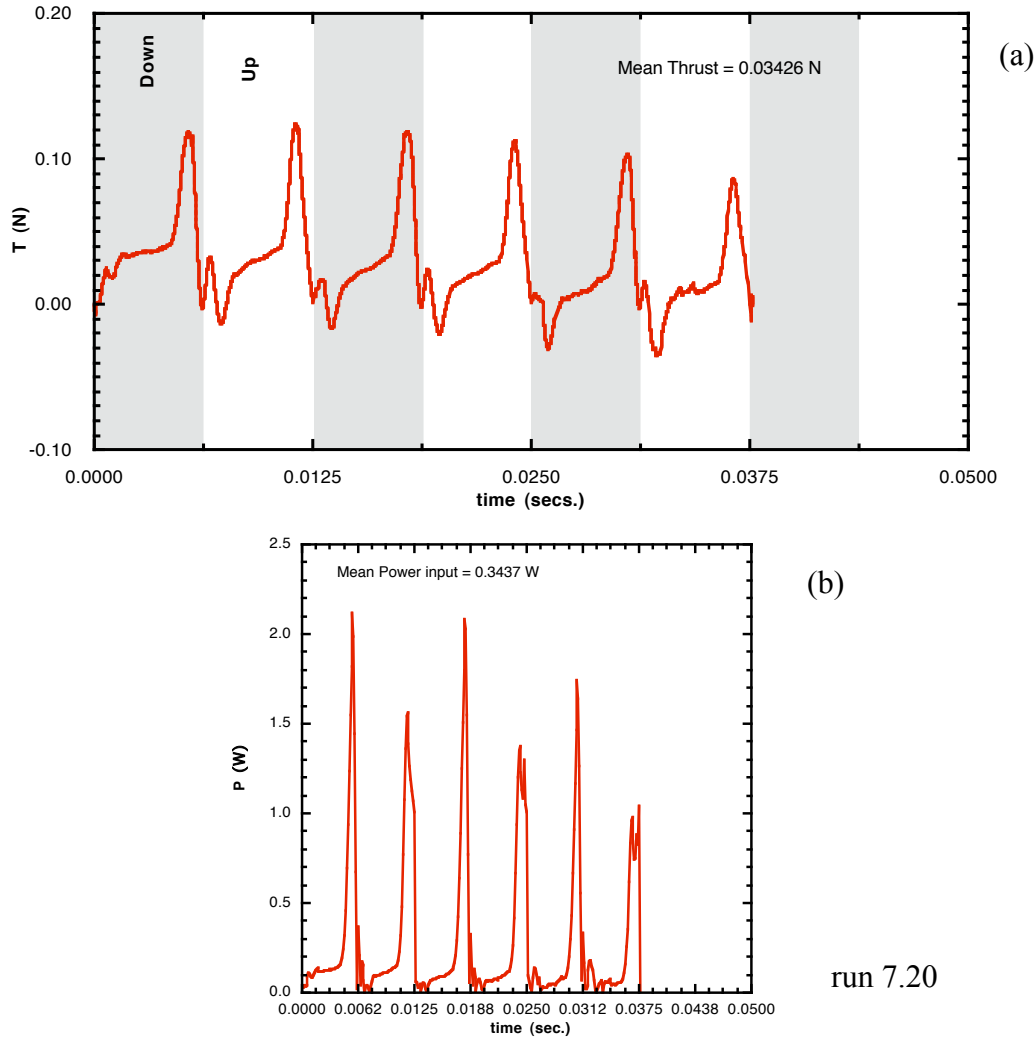


Fig. 50. Thrust production and aerodynamic power input to the flapping blade with modified stroke, $f = 80.0\text{Hz}$.

The secondary effort was more of a fundamental nature, in order to understand the differences between a rotating helicopter blade and a similarly designed wing undergoing a flapping motion. We found that an optimally designed propeller blade was able to operate with an FOM of 60% while the similarly shaped wing flapping at the same frequency attained only an overall FOM of 25%. Nevertheless, the flapping wing at the same frequency as the rotating propeller was able to generate 70% higher thrust. Again, the lower efficiency values are due to the continuous acceleration and deceleration of the flow. Also, the flapping propeller blade attains a similar FOM of 60% during the midstroke of the cycle. This suggests that the propeller blade which was optimized for the midstroke angle of attack was not well suited at the stroke reversals, during which the wing undergoes large changes in the angle of attack. The question of whether or not a flapping wing in hover is necessarily less efficient than a helicopter propeller is still open due to the fact that certain kinematic patterns have to be picked. It is not clear if poorer performance is fundamental to flapping or an artifact of the chosen kinematics. Further studies are needed to eliminate the adverse effects of vorticity shedding seen at stroke reversals.

Another study that is pertinent to hovering vehicles with flapping wings, is to employ a four-winged configuration similar to that of a Dragonfly. This opens up an area to investigate the effect of the phasing of the hind wing with respect to the forewing in order to augment the performance.

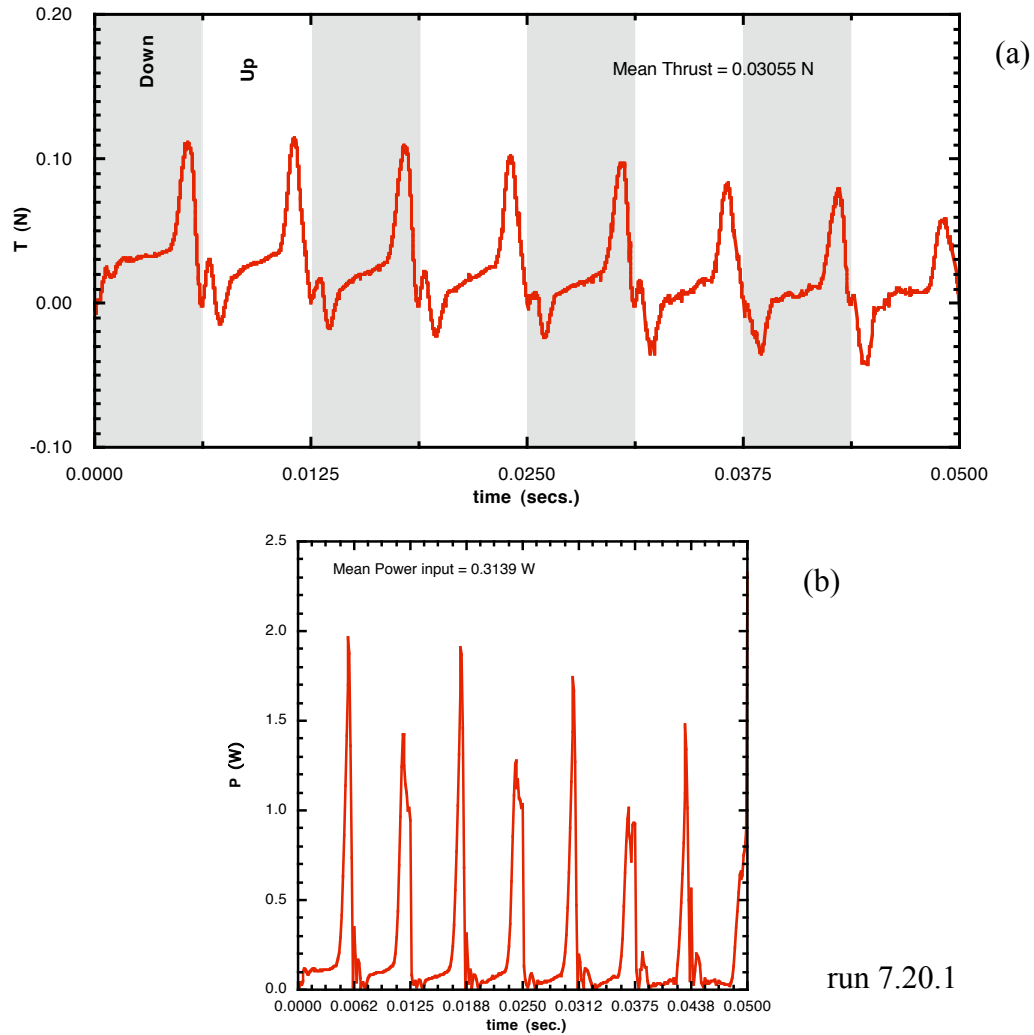


Fig. 51. Thrust production and aerodynamic power input to the flapping blade, $Re = 12,200$.

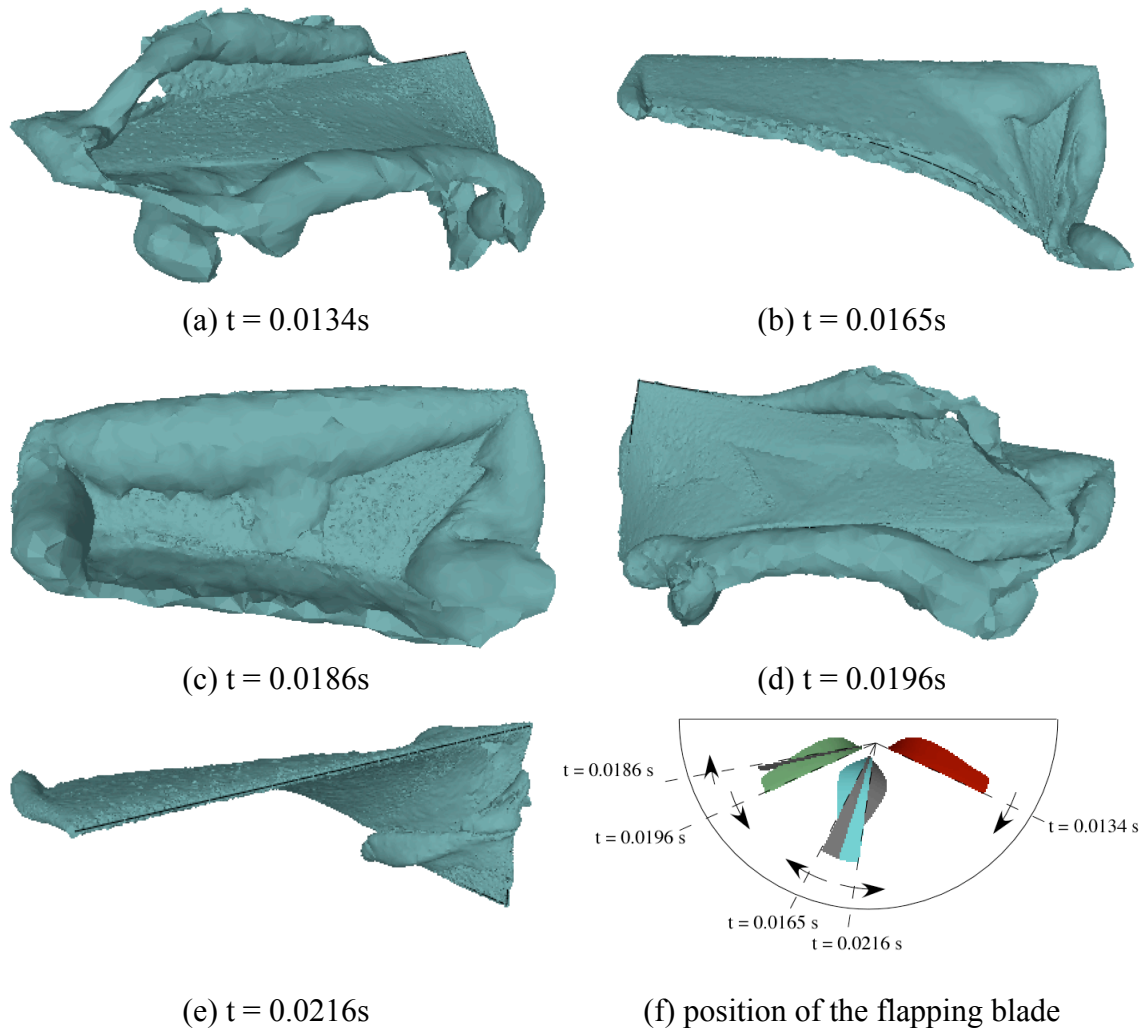


Fig. 52. Iso-vorticity contours during a flapping cycle, $f = 80$ Hz.

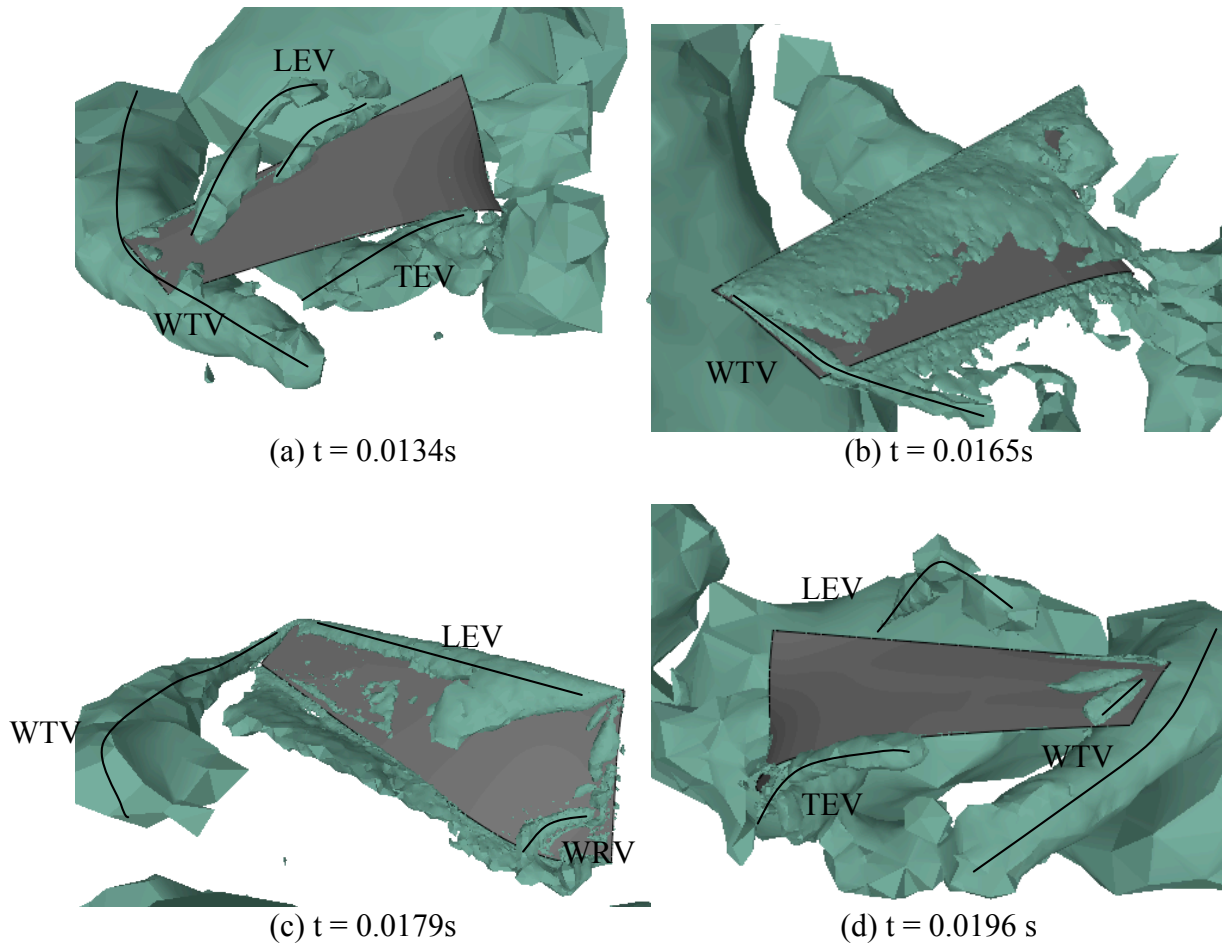


Fig. 53. Vortical activity in the flow depicted by the leading edge vortex (LEV), trailing edge vortex (TEV) and wing tip vortices (WTV). Iso-contours of the second invariant of $\nabla \mathbf{v}$ are shown.

Acknowledgements

This work was supported by the DARPA Nano Air Vehicle project through a contract with MicroPropulsion, Inc., with Anita Flynn as the Primary Investigator. The authors wish to thank the Team MicroPropulsion members, David Cylinder of PPPL, Steve Morris of MLB, Will Dickson and Michael Dickinson of Caltech, Ken Hall of Duke, Selden Crary of Cray Group and Rob Player of Boston Dynamics, for the many useful discussions throughout the course of this effort. Computational time for this work was supported in part by a grant of HPC time from the DoD HPC center at NRL.

References

1. Ramamurti, R. and Sandberg, W.C., Simulation of Flow about Flapping Airfoils using a Finite Element Incompressible Flow Solver, *AIAA J.*, Vol. 39, No. 2, 253-260, 2001.
2. Anderson, J.M., Vorticity Control for Efficient Propulsion, Ph. D. Dissertation, Massachusetts Institute of Technology, 1996.
3. Ramamurti, R. and Sandberg, W.C., A Three-Dimensional Computational Study of the Aerodynamic Mechanisms of Insect Flight, *J. Exp. Biol.*, Vol. 205, 10, pp. 1507-1518, May 2002.
4. Dickinson, M.H., Lehmann, F.-O. and Sane, S., Wing Rotation and the Aerodynamic Basis of Insect Flight, *Science*, Vol. 284, pp. 1954-1960, 1999.
5. Ramamurti, R. and Sandberg, W.C., A computational investigation of the 3-D unsteady aerodynamics of *Drosophila* hovering and maneuvering, *J. Exp. Biol.*, Vol. 210, No. 5, pp. 881-896, March 2007.
6. Fry, S.N., Sayaman, R. and Dickinson, M.H., The Aerodynamics of Free-Flight Maneuvers in *Drosophila*, *Science*, Vol. 300, 495-498, 2003.
7. Ramamurti, R., Sandberg, W.C., Vaiana, P., Kellogg, J. and Cylinder, D., Computational Fluid Dynamics Study of Unconventional Air Vehicle Configurations, *The Aero. J.*, Vol. 109, No., 1097, pp. 337-347, July 2005.
8. WebDOE. Web-based free Design of Experiments tool, Crary Group, <http://www.webdoe.com>, 2007.
9. Birch, J. and Dickinson, M.H., The influence of wing-wake interactions on the production of aerodynamic forces in flapping flight, *J. Exp. Biol.*, Vol. 206, 2257-2272, 2006.
10. Jeong, J. and Hussain, F., On the Identification of a Vortex, *J. Fluid Mech.*, Vol. 285, pp. 69-94, 1995.

Appendix**Table 2. Physical and Kinematic parameters for CFD simulations**

run #	Wing radius (m)	Radius of non-wash region (m)	Flapping Freq (Hz)	ϕ_{\max} - ϕ_{\min} (deg)	Chord Factor	γ factor	Phase Shift: β (deg)	Max. camber y_m
1.01	0.0425	0.0115	80.0	120.0	1.66667		0.00	0.000
1.1	0.0425	0.0115	80.0	120.0	1.30000		0.00	0.000
1.2.2	0.0369	0.0042	60.0	101.0	1.66667		0.00	0.000
1.2.3	0.0369	0.0042	60.0	101.0	1.66667		0.00	0.000
2.01	0.0375	0.0065	62.3	151.7	1.00000	1.00000	-15.30	0.000
2.02	0.0375	0.0065	62.3	151.7	1.00000	1.00000	0.00	0.000
2.03	0.0375	0.0065	62.3	151.7	1.00000	1.00000	15.30	0.000
2.04	0.0375	0.0065	62.3	151.7	1.00000	0.75000	-15.30	0.000
2.05	0.0375	0.0065	62.3	151.7	1.00000	0.75000	0.00	0.000
2.06	0.0375	0.0065	62.3	151.7	1.00000	0.75000	15.30	0.000
2.07	0.0375	0.0065	62.3	151.7	1.00000	0.50000	-15.30	0.000
2.08	0.0375	0.0065	62.3	151.7	1.00000	0.50000	0.00	0.000
2.09	0.0375	0.0065	62.3	151.7	1.00000	0.50000	15.30	0.000
5.01	0.0375	0.0065	62.3	151.7	1.25000	0.93745	15.30	4.485
5.02	0.0375	0.0065	62.3	151.7	1.25000	1.12500	-7.65	0.000
5.03	0.0375	0.0065	62.3	151.7	1.25000	0.62500	22.95	0.000
5.04	0.0375	0.0065	62.3	151.7	1.25000	1.00000	15.30	0.000
5.05	0.0375	0.0065	62.3	151.7	1.25000	1.25000	22.95	0.000
5.06	0.0375	0.0065	62.3	151.7	1.25000	0.62500	-7.65	0.402
5.07	0.0375	0.0065	62.3	151.7	1.25000	0.62500	22.95	10.000
5.08	0.0375	0.0065	62.3	151.7	1.25000	0.89846	22.95	4.993
5.09	0.0375	0.0065	62.3	151.7	1.25000	1.12500	7.65	10.000
5.10	0.0375	0.0065	62.3	151.7	1.25000	1.05925	22.95	10.000
5.11	0.0375	0.0065	62.3	151.7	1.25000	1.12500	-7.65	5.829
5.12	0.0375	0.0065	62.3	151.7	1.25000	0.62500	7.65	5.390
5.13	0.0375	0.0065	62.3	151.7	1.25000	0.89797	7.65	0.000
5.14	0.0375	0.0065	62.3	151.7	1.25000	0.74633	-7.65	10.000
5.15	0.0375	0.0065	62.3	151.7	1.25000	0.86646	7.65	5.019
5.09.1	0.0375	0.0065	62.3	151.7	1.25000	1.12500	7.65	0.000
5.10.1	0.0375	0.0065	62.3	151.7	1.25000	1.05925	22.95	0.000
5.04.1	0.0375	0.0065	72.5	151.7	1.25000	1.00000	15.30	0.000
5.04.2	0.0375	0.0065	62.3	151.7	1.22250	1.00000	15.30	0.000
5.04.3	0.0375	0.0065	62.3	151.7	1.66667	1.00000	15.30	0.000
5.04.4	0.0450	0.0065	62.3	151.7	1.55000	1.00000	15.30	0.000
6.01	0.0375	0.0065	62.3	151.7	1.25000	1.50000	15.30	0.000
6.02	0.0375	0.0065	62.3	151.7	1.25000	1.50000	0.00	0.000
6.03	0.0375	0.0065	62.3	151.7	1.25000	1.50000	-15.30	0.000
6.04	0.0375	0.0065	62.3	151.7	1.25000	1.50000	-30.60	0.000
6.05	0.0375	0.0065	62.3	151.7	1.25000	1.25000	-15.30	0.000
6.06	0.0375	0.0065	62.3	151.7	1.25000	1.25000	-15.30	4.000
7.01	0.0375	0.0065	62.3	120.0	1.25000		0.00	0.000
7.02	0.0375	0.0065	62.3	120.0	1.25250		0.00	0.000

run #	Wing radius (m)	Radius of non-wash region (m)	Flapping Freq (Hz)	ϕ_{\max} - ϕ_{\min} (deg)	Chord Factor	γ factor	Phase Shift: β (deg)	Max. camber y_m
7.03	0.0425	0.0115	62.3	120.0	1.25250		0.00	0.000
7.04	0.0375	0.0065	62.3	150.0	1.50000		0.00	0.000
7.05	0.0375	0.0065	62.3	151.7	1.00000	1.25000	-15.30	0.000
7.05.1	0.0375	0.0065	62.3	151.7	1.25000	1.25000	-15.30	0.000
7.05.2	0.0375	0.0065	62.3	151.7	1.50000	1.25000	-15.30	0.000
7.06	0.0375	0.0065	62.3	151.7	1.00000	1.25000	-15.30	0.000
7.06.1	0.0375	0.0065	62.3	151.7	1.25000	1.25000	-15.30	0.000
7.06.2	0.0375	0.0065	62.3	151.7	1.50000	1.25000	-15.30	0.000
7.07	0.0375	0.0065	62.3	160.0	1.50000	1.60000	0.00	0.000
7.08	0.0375	0.0065	62.3	151.7	1.25000	1.25000	-15.30	4.000
7.09	0.0375	0.0065	62.3	151.7	1.25000	1.25000	-15.30	4.000
prop	0.0375	0.0000	145.8	180.0	1.21050			
7.12	0.0375	0.0000	145.8	180.0	1.21050			
7.12.1	0.0375	0.0000	145.8	180.0	1.21050			
7.10	0.0375	0.0000	145.8	180.0	1.21050			
7.10	0.0375	0.0000	145.8	180.0	1.21050			
7.10	0.0375	0.0000	80.0	180.0	1.21050			
7.10	0.0375	0.0000	80.0	180.0	1.21050			
7.13	0.0375	0.0000	80.0	160.0	1.21050			
7.13	0.0375	0.0000	80.0	160.0	1.21050			
7.14	0.0375	0.0000	80.0	160.0	0.89193			
7.14	0.0375	0.0000	80.0	160.0	0.89193			
7.15	0.0375	0.0000	80.0	180.0	1.21050			
7.15	0.0375	0.0000	80.0	180.0	1.21050			
7.16	0.0375	0.0000	80.0	140.0	1.21050			
7.16	0.0375	0.0000	80.0	140.0	1.21050			
7.17	0.0375	0.0000	80.0	180.0	1.21050			
7.17	0.0375	0.0000	80.0	180.0	1.21050			
7.18	0.0375	0.0000	80.0	180.0	0.89193			
7.18	0.0375	0.0000	80.0	180.0	0.89193			
7.19	0.0375	0.0000	80.0	160.0	0.89193			
7.19	0.0375	0.0000	80.0	160.0	0.89193			
7.20	0.0375	0.0000	80.0	160.0	0.89193			
7.20	0.0375	0.0000	80.0	160.0	0.89193			
7.20.1	0.0375	0.0000	80.0	160.0	0.89193			
7.20.1	0.0375	0.0000	80.0	160.0	0.89193			
7.21	0.0375	0.0000	80.0	160.0	0.89193			
7.21	0.0375	0.0000	80.0	160.0	0.89193			
dros/run14	0.0023	0.0000	211.3	156.6		left wing		0.000
dros/run14	0.0023	0.0000	211.3	157.8		right wing		0.000
dros/run14	0.0023	0.0000	211.3	314.4		both wings		0.000

Table 3. Results from CFD simulations

run #	Mean Thrust T per wing (N)	P _{aero} per wing (W)	Freq. required for thrust (w two wings) equal to weight – f_{10} (Hz)	P _{aero} for two wings, scaled to f_{10}	A _{swept} (m ²)	Induced power (W)	Figure of merit
1.01	6.2600E-02	1.0100E+00	70.78	1.3989	0.00351	0.3344	23.91%
1.1	4.8100E-02	5.9910E-01	80.74	1.2320	0.00351	0.3344	27.15%
1.2.2	1.3098E-02	1.1471E-01	116.05	1.6601	0.00237	0.4069	24.51%
1.2.3	1.3533E-02	1.1424E-01	114.17	1.5741	0.00237	0.4069	25.85%
2.01	2.4900E-02	2.6620E-01	87.39	1.4697	0.00361	0.3295	22.42%
2.02	2.8400E-02	3.4790E-01	81.83	1.5769	0.00361	0.3295	20.90%
2.03	2.9400E-02	4.5500E-01	80.43	1.9580	0.00361	0.3295	16.83%
2.04	2.5300E-02	4.1300E-01	86.70	2.2263	0.00361	0.3295	14.80%
2.05	2.8000E-02	4.9600E-01	82.42	2.2965	0.00361	0.3295	14.35%
2.06	2.8700E-02		81.40		0.00361	0.3295	
2.07	2.0700E-02	5.6070E-01	95.85	4.0841	0.00361	0.3295	8.07%
2.08	2.2400E-02	6.2380E-01	92.14	4.0364	0.00361	0.3295	8.16%
2.09	2.1900E-02	6.7710E-01	93.19	4.5322	0.00361	0.3295	7.27%
5.01	3.9200E-02	6.6140E-01	69.65	1.8487	0.00361	0.3295	17.83%
5.02	2.9280E-02	2.9700E-01	80.59	1.2859	0.00361	0.3295	25.63%
5.03	3.1750E-02	8.6430E-01	77.40	3.3142	0.00361	0.3295	9.94%
5.04	3.6650E-02	6.1610E-01	72.04	1.9049	0.00361	0.3295	17.30%
5.05	3.1880E-02	5.6010E-01	77.24	2.1346	0.00361	0.3295	15.44%
5.06	3.2290E-02	6.7840E-01	76.75	2.5363	0.00361	0.3295	12.99%
5.07	3.4040E-02	8.9080E-01	74.75	3.0769	0.00361	0.3295	10.71%
5.08	3.8530E-02	7.6630E-01	70.26	2.1980	0.00361	0.3295	14.99%
5.09	3.8190E-02	4.7440E-01	70.57	1.3789	0.00361	0.3295	23.90%
5.10	3.9670E-02	6.6130E-01	69.24	1.8156	0.00361	0.3295	18.15%
5.11	3.2290E-02	2.9940E-01	76.75	1.1194	0.00361	0.3295	29.44%
5.12	3.5080E-02	7.9960E-01	73.63	2.6400	0.00361	0.3295	12.48%
5.13	3.7420E-02	6.0460E-01	71.29	1.8119	0.00361	0.3295	18.19%
5.14	3.7490E-02	6.0070E-01	71.22	1.7952	0.00361	0.3295	18.36%
5.15	3.9180E-02	6.2830E-01	69.67	1.7575	0.00361	0.3295	18.75%
5.09.1	3.3890E-02	4.5570E-01	74.91	1.5845	0.00361	0.3295	20.80%
5.10.1	3.5720E-02	6.4720E-01	72.97	2.0797	0.00361	0.3295	15.85%
5.04.1	4.9440E-02	9.7450E-01	72.18	1.9230	0.00361	0.3295	17.14%
5.04.2	3.2690E-02	4.1770E-01	76.27	1.5331	0.00361	0.3295	21.49%
5.04.3	4.8150E-02	7.6150E-01	62.85	1.5635	0.00361	0.3295	21.08%
5.04.4	7.9030E-02	1.5548E+00	49.06	1.5181	0.00525	0.2733	18.00%
6.01	2.2940E-02	4.1130E-01	91.05	2.5680	0.00361	0.3295	12.83%
6.02	1.8440E-02	2.2700E-01	101.56	1.9666	0.00361	0.3295	16.76%
6.03	1.1570E-02	9.8000E-02	128.21	1.7082	0.00361	0.3295	19.29%
6.04	6.5000E-03	5.1700E-02	171.05	2.1402	0.00361	0.3295	15.40%
6.05	2.1960E-02	1.6830E-01	93.06	1.1219	0.00361	0.3295	29.37%
6.06	2.4100E-02	1.6490E-01	88.83	0.9561	0.00361	0.3295	34.46%
7.01	1.4000E-02	1.3460E-01	116.55	1.7627	0.00286	0.3705	21.02%
7.02	1.5690E-02	1.2750E-01	110.10	1.4073	0.00286	0.3705	26.33%
7.03	2.2740E-02	2.0950E-01	91.45	1.3253	0.00351	0.3344	25.24%
7.04	3.1320E-02	3.0890E-01	77.92	1.2090	0.00357	0.3314	27.41%
7.05	2.1470E-02	1.6350E-01	94.12	1.1274	0.00361	0.3295	29.23%

run #	Mean Thrust T per wing (N)	P _{aero} per wing (W)	Freq. required for thrust (w two wings) equal to weight – f_{10} (Hz)	P _{aero} for two wings, scaled to f_{10}	A _{swept} (m ²)	Induced power (W)	Figure of merit
7.05.1	2.6210E-02	2.0900E-01	85.18	1.0685	0.00361	0.3295	30.84%
7.05.2	3.1390E-02	2.7270E-01	77.84	1.0637	0.00361	0.3295	30.98%
7.06	2.2330E-02	1.6160E-01	92.29	1.0506	0.00361	0.3295	31.37%
7.06.1	2.6760E-02	2.1920E-01	84.30	1.0863	0.00361	0.3295	30.34%
7.06.2	3.2070E-02	2.8990E-01	77.01	1.0950	0.00361	0.3295	30.09%
7.07	1.4020E-02	1.2940E-01	116.47	1.6910	0.00381	0.3209	18.98%
7.08	2.8910E-02	2.1900E-01	81.11	0.9665	0.00361	0.3295	34.10%
7.09	3.0480E-02	2.3000E-01	78.99	0.9376	0.00361	0.3295	35.15%
prop	5.4085E-02	3.2025E-01	138.81	0.5523	0.00442	0.2979	53.94%
7.12	8.3805E-02	5.0265E-01	111.51	0.4495	0.00442	0.2979	66.29%
7.12.1	7.4799E-02	4.7108E-01	118.03	0.4995	0.00442	0.2979	59.64%
7.10	1.7099E-01	6.2776E+00	78.07	1.9260	0.00442	0.2979	15.47%
7.10	1.0698E-01	1.0500E+00	98.70	0.6510	0.00442	0.2979	45.77%
7.10	4.7248E-02	9.7107E-01	81.47	2.0511	0.00442	0.2979	14.53%
7.10	3.1514E-02	1.5897E-01	99.76	0.6165	0.00442	0.2979	48.33%
7.13	3.7690E-02	7.8454E-01	91.22	2.3259	0.00393	0.3160	13.59%
7.13	2.8644E-02	1.3253E-01	104.63	0.5930	0.00393	0.3160	53.29%
7.14	4.4053E-02	5.6256E-01	84.37	1.3199	0.00393	0.3160	23.94%
7.14	3.5150E-02	1.4387E-01	94.45	0.4736	0.00393	0.3160	66.73%
7.15	5.9089E-02	1.7133E+00	72.85	2.5876	0.00442	0.2979	11.51%
7.15	4.1714E-02	2.2066E-01	86.71	0.5619	0.00442	0.2979	53.03%
7.16	3.8161E-02	1.8130E+00	90.65	5.2760	0.00344	0.3378	6.40%
7.16	7.1886E-02	1.3149E+00	66.05	1.4800	0.00344	0.3378	22.83%
7.17	2.7796E-02	3.6952E-01	106.22	1.7297	0.00442	0.2979	17.22%
7.17	2.6579E-02	1.3602E-01	108.62	0.6810	0.00442	0.2979	43.75%
7.18	1.7579E-02	4.0412E-01	133.56	3.7613	0.00442	0.2979	7.92%
7.18	2.0368E-02	1.1597E-01	124.08	0.8654	0.00442	0.2979	34.43%
7.19	4.6718E-02	7.1766E-01	81.93	1.5417	0.00393	0.3160	20.50%
7.19	4.3185E-02	3.8414E-01	85.22	0.9286	0.00393	0.3160	34.03%
7.20	3.4265E-02	3.4373E-01	95.67	1.1756	0.00393	0.3160	26.88%
7.20	3.0294E-02	1.3464E-01	101.74	0.5539	0.00393	0.3160	57.05%
7.20.1	3.0555E-02	3.1388E-01	101.31	1.2749	0.00393	0.3160	24.79%
7.20.1	2.6597E-02	1.1719E-01	108.58	0.5861	0.00393	0.3160	53.92%
7.21	4.3312E-02	4.7575E-01	85.09	1.1450	0.00393	0.3160	27.60%
7.21	4.9317E-02	3.5886E-01	79.74	0.7108	0.00393	0.3160	44.46%
dros/run14	6.4210E-06	1.3355E-05			1.44585E-05	2.7621E-06	20.68%
dros/run14	6.4920E-06	1.3543E-05			1.45647E-05	2.7978E-06	20.66%
dros/run14	1.2913E-05	2.6898E-05			2.90233E-05	5.5598E-06	20.67%

